Evaluating CHASER V4.0 global formaldehyde (HCHO) simulations using satellite, aircraft, and ground-based remote sensing observations

Hossain Mohammed Syedul Hoque[1], Kengo Sudo[1,2], Hitoshi Irie[3], Yanfeng He[1], and Md Firoz Khan[4]

[1]Graduate School of Environmental Studies, Nagoya University, Nagoya, 4640064, Japan

[2]Japan Agency for Marine-Earth Science and Technology (JAMSTEC), Kanagawa, 2370061, Japan

[3]Center for Environmental Remote Sensing (CEReS), Chiba University, Chiba,2638522, Japan

[4]Department of Environmental Science and Management, North South University, Bangladesh

Correspondence to: Hossain Mohammed Syedul Hoque (hoquesyedul@gmail.com; hoque.hossain.mohammed.syedul.u6@f.mail.nagoya-u.ac.jp)

Abstract

Formaldehyde (HCHO), a precursor to tropospheric ozone, is an important tracer of volatile organic compounds (VOCs) in the atmosphere. Two years of HCHO simulations obtained from the global chemistry transport model CHASER at a horizontal resolution of 2.8° × 2.8° have been evaluated using observations from the Tropospheric Ozone Monitoring Experiment (TROPOMI), Atmospheric Tomography Mission (ATom), and multi-axis differential optical absorption spectroscopy (MAX-DOAS) observations. CHASER reproduced the observed global HCHO spatial distribution with a spatial correlation (*r*) of 0.93 and a negative bias of 7%. The model showed good capability for reproducing the observed magnitude of the HCHO seasonality in different regions, including the background conditions. The discrepancies between the model and satellite in the Asian regions were related mainly to the underestimated and missing anthropogenic emission inventories. TROPOMI's finer spatial resolution than that of the Ozone Monitoring Experiment (OMI) sensor reduced the global model–-satellite root-mean-square-error (RMSE) by 20%. The OMI and TROPOMI observed seasonal variations in HCHO abundances were consistent. However, the simulated seasonality showed better agreement with TROPOMI in most regions. The simulated HCHO and isoprene profiles correlated strongly (R = 0.81) with the ATom observations. CHASER overestimated HCHO mixing ratios over dense vegetation areas in South America and the remote Pacific (background condition) regions, mainly within the planetary boundary layer (<2 km). The simulated temporal (daily and diurnal) variations in the HCHO mixing ratio

showed good congruence with the MAX-DOAS observations and agreed within the 1-sigma standard deviation of the observed values.

1 Introduction

Formaldehyde (HCHO), the most abundant carbonyl compound in the atmosphere, is a high-yield oxidation product of all primary biogenic and anthropogenic non-methane volatile organic compounds (NMVOCs). Methane (CH_4) oxidization produces background HCHO concentrations of 0.2–1.0 ppbv (Burkert et al., 2001; Singh et al., 2004; Sinreich et al., 2005; Weller et al., 2000). Along with secondary sources (i.e., oxidization of NMVOCs), biomass burning, industrial processes, and fossil fuel combustions are primary HCHO emission sources (Fu et al., 2008; Hak et al., 2005; Lee et al., 1997). However, the oxidization of NMVOCs drives the spatial variability of HCHO on a global scale (Franco et al., 2015). The HCHO removal mechanisms include photolysis at wavelengths below 400 nm, oxidization by hydroxyl radicals (OH), and wet deposition. The atmospheric lifetime of HCHO is around a few hours (Arlander et al. 1995). Therefore, HCHO observations can help elucidate chemical processes in the atmosphere. A few examples are the following: (1) the ozone (O_3) production regime can be determined from the HCHO to nitrogen dioxide (NO_2) ratio (Hoque et al., 2022); (2) midday OH levels can be quantified from the oxidation of isoprene into HCHO (Kaisar et al., 2015); and (3) HCHO, being an intermediate product in oxidation chain of NMVOCs, engenders the formation of carbon monoxide (CO) and carbon dioxide (CO_2). Consequently, CO chemical production from NMVOCs and CH_4 can be quantified from HCHO measurements (De Smedt et al., 2021).

Given its importance, global HCHO observations started in 1995 with the launch of the nadir viewing ultraviolet (UV) sensor Global Ozone Monitoring Experiment (GOME; Burrows et al., 1997). Since then, numerous sensors have succeeded: SCanning Imaging Absorption Spectrometer for Atmospheric CHartographY (SCIAMACHY; De Smedt et al., 2008, 2010; Wittrock et al., 2006) onboard the ENVISAT satellite, Ozone Monitoring Instrument (OMI) (Levelt et al., 2018), Global Ozone Monitoring Experiment – 2 (GOME-2) (Munro et al., 2016), and Ozone Mapping and Profiler Suite (González Abad et al., 2016, new reference). The HCHO observations from these sensors have been used extensively to evaluate models, air quality, and climate change (De Smedt et al., 2010, 2012, 2015; Hoque et al., 2022).

The Tropospheric Ozone Monitoring Instrument (TROPOMI) (De Smedt et al., 2021; Veefkind et al., 2012), launched on the European Copernicus Sentinel-5 Precursor (S5P) satellite on October 13, 2017, is the recent addition to the series of nadir viewing UV sensors providing HCHO data. The unprecedented original spatial resolution of 3.5×7 km^2 (across-track × along-track) refined to 3.5×5.5 km^2 on August 6, 2019, is the crucial feature of TROPOMI. Such spatial resolution is almost 16 times finer than its predecessor, OMI (De Smedt et al., 2021). Such high-resolution observations will likely reduce uncertainties in the HCHO products for multiple research purposes.

Several studies using the TROPOMI HCHO product have been reported in the literature. De Smedt et al. (2021) and Vigouroux et al. (2020) have respectively validated TROPOMI HCHO against MAX-DOAS and FTIR networks comprehensively. Both studies have concluded that TROPOMI HCHO products have achieved the pre-launch accuracy requirement of < 40–80%. Ryan et al. (2021) and Chan et al. (2020) respectively reported good agreement between TROPOMI and MAX-DOAS in Melbourne and Munich. In addition to validation studies, HCHO products have been used to infer changes in the global HCHO levels during the COVID-19 pandemic-led shutdown (Level et al., 2022; Souri et al., 2021; Su et al., 2021).

Among the multitude of applications of TROPOMI HCHO observations, few efforts have specifically evaluated HCHO simulations from global chemistry transport models (CTMs). This work evaluates the global Chemical Atmospheric General Circulation Model for the Study of Atmos. Environ. and Radiative Forcing (CTM CHASER) (Sekiya & Sudo, 2014; Sudo et al., 2002, 2007) simulated HCHO spatiotemporal distribution against TROPOMI HCHO observations. In addition, airborne and ground-based observations are used to validate the simulated HCHO profiles and surface mixing ratios in a few regions. CHASER simulations of NO_2, OH, and O_3 have been evaluated against satellite and ground-based observations (e.g., Sekiya & Sudo, 2014; Sekiya et al., 2018). Moreover, CHASER is a forward model in the chemical reanalysis system (TCR) developed by Miyazaki et al. (2017, 2020). The model simulations are performed at a horizontal resolution of 2.8° × 2.8° (T42). Although the model can run at

higher resolutions, T42 is the most commonly used framework for CHASER applications. Therefore, it is used for this study.

2 Model, observations, and methods

2.1 CHASER

CHASER 4.0 (ver. 4) is a global CTM that studies the atmospheric enviroment and radiative forcing. It is coupled online with the MIROC atmospheric general circulation model (AGCM) and the SPRINTAS aerosol transport model (Takemura et al., 2005, 2009). The latest version of CHASER entails several updates, including the formation of aerosol species and related chemistry, radiation, and cloud processes.

Through 263 multi-phase (gaseous, aqueous, and heterogenous) chemical reactions, CHASER calculates the concentrations of 92 species considering the chemical cycle of O_3 – NO_x (nitrogen oxides) – HO_x (hydrogen oxides) -CH_4-CO along with oxidation of NMVOCs (Ha et al., 2023; He et al., 2022; Hoque et al., 2022; Miyazaki et al., 2017; Sekiya et al., 2023). The chemical mechanism is adopted mainly from the master chemical mechanism (MCM) (Jenkin et al., 2015). The stratospheric O_3 chemistry simulations are based on the Chapman mechanisms, the catalytic reaction of halogen oxides, and polar stratospheric clouds. The dry and wet depositions are calculated based on resistance-based parameterization (Wesley et al., 1984), cumulus convection, and large-scale condensation parameterization. Advective trace transport is calculated using the piecewise parabolic method (Colella & Woodward, 1984) and flux-form semi-Lagrangian schemes. Tracer transport is simulated on a sub-grid scale in the framework of the prognostic Arakawa–Schubert cumulus convection scheme (Emori et al., 2001) and vertical diffusion scheme (Mellor & Yamada, 1974). The simulations were performed at horizontal resolution of 2.8° × 2.8°, with 36 vertical layers from the surface to approx. 50 km altitude, with a 20 min time step. At every time step, meteorological fields obtained from the MIROC AGCM were nudged toward the 6-hourly NCEP FNL reanalysis data.

CHASER incorporates emissions from biomass burning, anthropogenic sources, lightning, and soil. Anthropogenic emissions are obtained from the HTAP_v3 (Crippa et al, 2023). Reanalysis data from the ECMWF MACC (Global Fire Assimilation System, GFAS) were used for biomass burning and soil emissions. Biogenic emissions of VOCs are obtained from a process-based biogeochemical model: the Vegetation Integrative Simulator for trace gases (VISIT) (Ito and Inatomi, 2012). Lightning NO_x production estimates are based on the parameterization of Price and Rind (1992) and linked to the convection scheme of the AGCM. Global NO_x emissions in CHASER are set to 43.80 TgN/yr considering industrial production (23.10 TgN /yr), biomass burning (9.65 TgN/yr), soil (5.50 TgN /yr), lightning (5 TgN/yr), and aircraft (0.55 TgN/yr) as significant emission sources. Global isoprene emissions are set as 400 TgC/yr. Annual monoterpene, acetone, and other non-methane volatile organic compound (ONMV) emissions are, respectively, 102, 20, and 60 TgC/yr. Direct emissions of HCHO from anthropogenic sources and biomass burning are not considered in CHASER. However, secondary production of HCHO

from VOCs (C_2H_6, C_3H_8, C_2H_4, C_3H_6, CH_3COCH_3, ONMV) emitted directly from anthropogenic and pyrogenic sources is considered.

CHASER simulated NO_2 and OH spatiotemporal variability showed good agreement with OMI and ATom observations, respectively (Sekiya et al., 2018). The quality of O_3 simulations has been explained in the work of Sudo et al., (2014). Ha et al., (2023) and He et al., (2022) updated the heterogenous chemistry and lightning NO_x scheme, respectively. These updates have not been considered in the current study. The effect of these updates on the HCHO simulations will be addressed in a separate study. Multiple simulations with varying emission inputs were performed for the study. They are presented in Table 1.

Table 1. Combinations of emission inventories for different simulations used in this study

Simulation name	NO_X emissions	Biogenic emissions	Anthropogenic VOC emissions	Biomass burning
Standard	HTAP_v3	ON	ON	ON
ANI	HTAP_v3	ON	Increased three-fold	ON
OLNE	HTAP_v2.2	ON	ON	ON

To account for the altitude dependence of TROPOMI observations, averaging kernel (AK) information obtained from the level 2 (L2) files was applied to all simulations following the method of Sekiya et al., (2018). First, the simulated HCHO profiles were sampled closest to the TROPOMI overpass of 13:30 LT (Local Time). Secondly, AKs averaged on a 2.8° bin grid were applied to the sampled profiles. Then the total column was calculated. The model vertical grids were interpolated to the TROPOMI vertical grids to account for the differences in the vertical grids. Thirdly, the AK-applied model columns on the available measurement days were selected. Lastly, the observational dataset was averaged on a 2.8° bin grid.

2.2 TROPOMI

The TROPOMI operational L2 HCHO vertical column density (VCD) (ver. 1.1.5.7) data from 2019 to 2020 have been used for this study. A continuous record of reprocessed and offline data since May 2018 has been included in this product. The S5P TROPOMI HCHO L2 product user manual (Veefkind et al., 2012) provides a detailed product description. The TROPOMI HCHO retrieval algorithm is based on the DOAS technique, adapted directly from the OMI QA4ECV product retrieval algorithm (De Smedt et al., 2017). The three-step retrieval algorithm was explained explicitly by De Smedt et al. (2018). Slant columns were retrieved from the UV part of the spectra (Channel 3) in a 328.5–358 nm fitting window. The HCHO cross-section data reported by Meller and Moortgart (2000) were used for fitting the spectra.

All the cross-sections were convolved with the instrument slit function (adjusted after the launch) for every row separately. Spectra averaged over the tropical Pacific region from the prior day were used as reference spectra for the DOAS fit (De Smedt et al., 2021; Vigouroux et al., 2020). The slant columns therefore exceed the average Pacific background HCHO levels because they were derived from the local and reference spectrum differences. The slant columns were converted to tropospheric columns (Nv) using a look-up table of vertically resolved air mass factors (*M*) at 340 nm calculated with the radiative transfer model VILDORT v2.6 (Spurr, 2008). The value of *M* depends on the observation geometry, surface albedo, cloud properties, and a priori profiles of HCHO. The surface albedo at spatial resolution of 1° × 1° was extracted from the monthly OMI albedo climatology (Kleipool et al., 2008). Daily HCHO a priori profiles were obtained from TM5-MP CTM at a similar spatial resolution. The independent pixel approximation (Boersma et al., 2004) approach was applied to pixels with cloud fractions greater than 0.1. Background correction was performed based on HCHO slant columns from the five prior days over the Pacific Ocean to account for any remaining global offsets and stripes (De Smedt et al., 2021). Background HCHO contribution from CH_4 oxidation in the reference region is calculated with TM5-MP. The resulting HCHO tropospheric column is calculated using equation (1):

$$N_v = \frac{N_s - N_{s,o}}{M} + \frac{M_o}{M} * N_{v,0}^{CTM} \qquad (1)$$

where M_o is the air mass factor of the reference sector. Following De Smedt et al. (2021), the following filters ensured the data quality: (1) cloud fraction less than 0.3, (2) quality assurance values greater than 0.5, (3) retrievals with solar zenith angle (SZA) less than 70°, (4) surface albedo less than 0.1, and (5) air mass factor greater than 0.1. Total uncertainty in the reprocessed TROPOMI HCHO columns was estimated as >= 90% for the fire-free region (Zhao et al., 2022, and references therein). The uncertainties in the air mass factors, slant column fitting, and background HCHO respectively account for 75, 25, and 40% of the total uncertainty. The estimated uncertainty in the retrievals in regions with strong fires is ~35%.

2.2 OMI

The comparison study used HCHO retrievals from OMI: a nadir-viewing spectrometer on board the Aura satellite, which measures backscattering solar radiation in the spectral range of 270–500 nm (Levelt et al., 2018). OMI crosses the equator at 13:40 LT (Zara et al., 2018) and provides daily global coverage of trace gases, including HCHO, at spatial resolution of 13 × 24 km^2. For use in this study, HCHO columns from 2019 to 2020, retrieved using the BIRA-IASBv14 (De Smedt et al., 2021), were obtained from the Aeronomie website (i.e., https://www.temis.nl/qa4ecv/hcho/hcho_omi.php, last accessed on 01/07/2023). The data-filtering criteria were cloud fraction < 0.3, SZA < 70˚, quality flag =0, and cross-track quality flag = 0.

2.4 ATom-4 aircraft campaign

The NASA Atmospheric Tomography (ATom) mission used a DC-8 aircraft to study the remote atmosphere over the Pacific and Atlantic oceans from ~80° N to ~65° S (Wofsy et al., 2018). Repeated

flights measured the vertical profiles from 0.15 to 12 km to provide information related to greenhouse gases, reactive and tracer species, and aerosol composition and size distribution (Kupc et al., 2018). Over two years and four phases, sampling was conducted in one of the four seasons in each stage (Zhao et al., 2022). Here, the 1-minute averaged measurements of HCHO and isoprene during the ATom-4 flight (Fig.S2) in 2018 are used for the model evaluation. The NASA In Situ Airborne Formaldehyde (ISAF) instrument (Cazorla et al., 2015) performed HCHO sampling based on the laser-induced fluorescence technique. Isoprene was measured using two instruments: (a) The University of Irvine Whole Air Sampler (WAS) and (b) the National Center for Atmospheric Research (NCAR) Trace Organic Gas Analyzer (TOGA). WAS sampled the air every 3–5 min, with subsequent analyses in the laboratory using gas chromatography (Simpson et al., 2020). TOGO sampling was conducted every 2 min with a 35 s integrated sampling time (Apel et al., 2021). The uncertainty in the WAS and TOGO isoprene observations are, respectively ±10 and 15%. Measurement uncertainties in HCHO were reported as 10%. The simulations have been interpolated to the observed spatial and temporal resolution following the method of He et al., (2022). The observed and interpolated HCHO and isoprene vertical profiles were averaged over a 300-meter bin.

2.5 MAX-DOAS observations

HCHO columns and the volume mixing ratio (vmr) were retrieved from two-year (2019–2020) MAX-DOAS observations at Phimai (15.18°N, 102.46°E, 212 m a.s.l.), Chiba (35.62°N, 140.10°E, 21 m a.s.l.), and Kasuga (33.52°N, 130.47°E, 28 m a.s.l.). The MAX-DOAS observations were conducted under the framework of the international air quality and sky research remote sensing (A-SKY) network (Irie, 2021). Phimai is a rural site in Thailand and experiences biomass burning influence from January to April. The climate is divided into two seasons- (1) dry season (January to May) and (2) wet season (June to December). Chiba and Kasugai are urban sites in central and southern Japan, respectively. The seasonal classification at these sites is – Spring (March to May), Summer (June to August), Autumn (September to November) and winter (December to February). The observations at these sites are described elsewhere (i.e., Hoque et al., 2018a; Irie et al., 2011,2015).

The A-SKY MAX-DOAS system, including the instrument and algorithm, participated in the Cabauw Intercomparison campaign for Nitrogen Dioxide measuring Instruments (CINDI) and CINDI-2 (Kreher et al., 2020; Roscoe et al., 2010) campaigns. The instrumentation has been described explicitly by Irie et al. (2008, 2011, 2015). A UV spectrometer (Maya2000Pro; Ocean Insight, Inc.) recorded high-resolution spectra from 310–515 nm at six elevation angles (ELs) of 2°, 3°, 4°, 6°, 8° and 70°, which were repeated every 15 min. The reference spectra were recorded at EL of 70° instead of 90° to avoid saturation intensity. Spectra measured at all ELs were considered in the retrieved vertical profile and total columns. Consequently, the choice of reference ELs has no appreciable effect on the retrieval. The systematic error in the oxygen collision complex (O_4) was reduced by limiting the off-axis ELs to less than 10° (Irie et al., 2015). However, this limitation reduces sensitivity above the planetary boundary layer (PBL), maintaining high sensitivity in the lower layers of the retrieved profiles. The high-resolution solar spectrum measured by Kurucz et al. (1984) was used for daily wavelength calibration. The spectral resolution is approximately 0.4 nm at 357 and 476 nm (Hoque et al., 2022). Aerosol and trace gas columns

and profiles were retrieved using the Japanese vertical profile retrieval algorithm JM2 (ver. 2) (Irie et al., 2011, 2015). Three-step profile and column retrievals by JM2 are explained explicitly in earlier reports (e.g., Hoque et al., 2018; Irie et al., 2011, 2015). The estimated total error (random and systematic) in the HCHO product is 30% (Hoque et al., 2022). Following Irie et al. (2011) and Hoque et al. (2018a, 2022), cloud screening was performed to ensure data quality.

3 Results and discussion

3.1 Global and regional comparison

Figure 1 presents a comparison of global distributions of annual mean HCHO columns obtained from TROPOMI retrievals and standard CHASER simulations at the TROPOMI overpass time (13:30). Differences between the observations and model simulations in the respective years are also depicted. The statistics related to the comparison are presented in Table 2. The simulation results agree well with the TROPOMI observations, with a global spatial correlation (r) of 0.93, mean bias error (MBE) (CHASER–TROPOMI) of -0.20×10^{15} molecules cm^{-2}, and root-mean-square error (RMSE) of 0.75×10^{15} molecules cm^{-2}. The r, MBE, and RMSE values between 60° S and 60° N were, respectively, 0.92, 0.13×10^{15} molecules cm^{-2}, and 0.82×10^{15} molecules cm^{-2}. CHASER HCHO columns are negatively biased relative to the TROPOMI retrievals. Table S2 shows the MBE and RMSE values obtained for the individual months. No seasonal variation in the systematic differences was observed between CHASER and TROPOMI. Biases can originate from uncertainties in the retrieval and model assumptions. TROPOMI HCHO retrievals greater than 8×10^{15} molecules cm^{-2} were negatively biased by 25% relative to the ground-based MAX-DOAS observations (De Smedt et al., 2021), whereas direct emissions of HCHO were not considered in CHASER.

TROPOMI and CHASER show high HCHO concentrations over South America, central Africa, India, eastern China, and Southeast Asia. Simulated HCHO magnitudes in the hotspot regions were $0.8–1.4 \times 10^{16}$ molecules cm^{-2}, slightly higher than the observed range of $0.8–1 \times 10^{16}$ molecules cm^{-2}. The dataset's greatest differences (~4×10^{15} molecules cm^{-2}) were observed over Brazil and Southeast Asia. The datasets show strong congruence in the high-latitude regions. The simulated and observed HCHO columns over Europe, the Middle East, Japan, and Russia were $0.3–0.6 \times 10^{16}$ molecules cm^{-2}. Simulated HCHO columns (~3×10^{15} molecules cm^{-2}) over the remote Pacific region were consistent with the observations, too. The remote Pacific regions represent background conditions strongly linked to CH_4

oxidation. Congruence with observations in this region suggests that the simulated CH_4 estimates in the remote areas are reasonable.

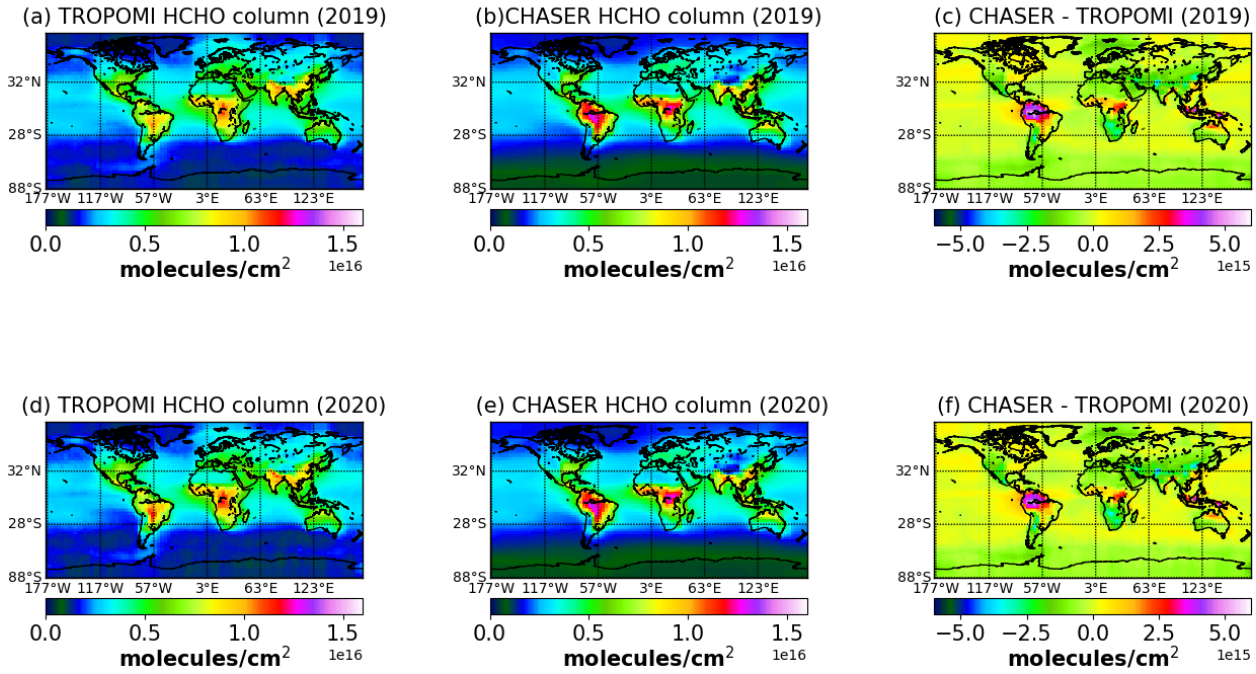

Figure 1. Annual mean HCHO columns ($\times 10^{16}$ molecules cm^{-2}) in 2019 and 2020 were obtained from TROPOMI retrievals (first column) and standard CHASER simulation (second column). The differences between the model and observations in the respective years are shown in the third column. The unit of difference is $\times 10^{15}$ molecules cm^{-2}.

Table 2. Comparison of annual mean HCHO ($\times 10^{16}$ molecules cm^{-2}) column between TROPOMI retrievals and CHASER simulations in 2019 and 2020. MBE and RMSE are the abbreviated forms of mean bias error and root mean square error, respectively. Units of MBE and RMSE are $\times$ 10^{15} molecules cm^{-2}. Correlation signifies the spatial correlation between the datasets.

Year	Correlation	MBE	RMSE
2019	0.93	-0.20	0.75
2020	0.93	-0.19	0.75

Figure 2 presents a comparison of the observed and simulated seasonality in HCHO columns ($\times 10^{16}$ molecules $cm^{-2)}$ in different regions. The MBE ($\times 10^{15}$ molecules cm^{-2}) between TROPOMI and CHASER HCHO columns in each region is shown in blue. The statistics of the comparison are given in Table 3.

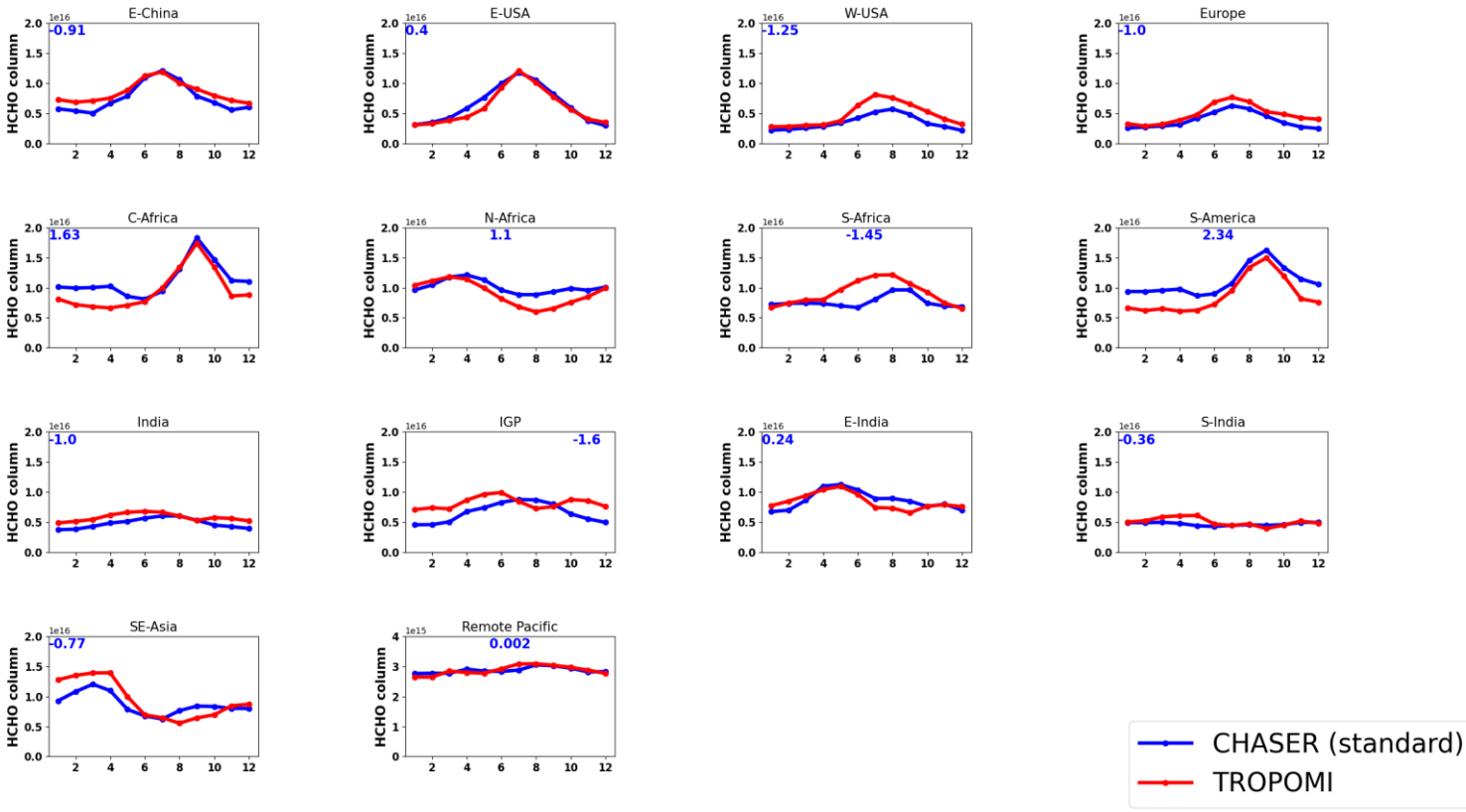

Figure 2. Seasonal variation in HCHO columns ($\times 10^{16}$ molecules cm^{-2}) in eastern China (E-China; 30–40°N, 110–123°E), eastern United States (E-USA; 32–43°N,95–71°W), western United States (W-USA; 32–43°N, 125–100°W), Europe (35–60°N, 0–30°E), central Africa (C-Africa; 10–20°S, 60°W – 60°E), northern Africa (N-Africa; 5–15°N, 10°W–30°E), southern Africa (S-Africa; 5–15°S, 10–30°E), South America (S-America; 20°S – 0°N, 50–70° W), India (7.5–54°N, 68–97°E), the Indo Gangetic Plain (IGP; 21–33°N, 72–89°E), east India (E-India; 15–25°N, 80–90°E)), south India (S-India; 0–15°N, 63–80°E), Southeast Asia (SE-Asia, 10–20°N, 96–105°E), and the remote Pacific region (28°S – 32°N, 117°–177°W) as inferred from CHASER simulations (blue) and TROPOMI observations (red). Blue numbers denote MBE between the TROPOMI and CHASER HCHO columns.

(a) E-China

Over E-China, the datasets are moderately correlated (r =0.44), with MBE and RMSE values of -0.9 and 1.62 × 10^{15} molecules cm^{-2}, respectively. The simulated seasonality correlates strongly with the observations (R= 0.97), with a consistent peak (1 × 10^{16} molecules cm^{-2}) in the HCHO variability in July. The HCHO columns' peaks are compatible with the peak in isoprene concentrations (Fig. S3), manifesting a strong biogenic contribution during summer. CHASER mostly underestimated the winter-time HCHO columns in this region. Liu et al. (2021) reported vehicular exhaust, solvent usage, and combustion-related regional transport as the primary VOC emission sources during winter in Shanghai, a megacity in eastern China. Consequently, the model's missing or underestimated anthropogenic HCHO emissions is one of the potential reasons for the discrepancy.

Table 3: Comparison of monthly mean tropospheric HCHO (× 10^{16} molecules cm^{-2}) columns obtained from TROPOMI retrievals and standard CHASER simulations. Coincident dates in 2019 and 2020 are used to calculate the statistics. Units of MBE and RMSE are × 10^{15} molecules cm^{-2}.

Region	MBE (model – TROPOMI)	RMSE (model – TROPOMI)	Spatial Correlation (*r*-value)	Temporal Correlation (*R*-value)
E-China	-0.91	1.62	0.44	0.97
E – USA	0.40	0.43	0.97	0.97
W-USA	-1.25	1.29	0.85	0.95
Europe	-1.00	1.25	0.42	0.95
C-Africa	1.63	1.73	0.89	0.92
N-Africa	1.10	1.26	0.87	0.83
S-Africa	-1.45	1.64	0.89	0.59
S-America	2.34	2.85	0.56	0.97
India	-1.00	1.45	0.91	0.77
IGP	-1.60	1.99	0.91	0.44
E-India	0.24	1.08	0.86	0.72
S-India	-0.36	0.52	0.96	0.34
SE-Asia	-0.77	1.22	0.71	0.87

Remote Pacific	0.002	0.13	0.86	0.76

(b) Eastern USA, western USA, and Europe

CHASER has well-reproduced the HCHO spatial variability in the eastern USA (E-USA; r=0.97) and western USA (W-USA; r=0.85). The peaks in the HCHO variability coincide with the isoprene peak in these regions (Fig. S2). The simulated amplitude of the HCHO seasonal modulation in E-USA and W-USA are 74 and 62%, whereas the observed seasonal amplitudes are 74 and 65%, respectively. The peak in the HCHO seasonality in E-USA is similar in both datasets (~1.2×10^{16} molecules cm^{-2}). The RMSE value in the W-USA region is 15% higher than in E-USA. Although the spatial correlation in Europe is moderate (r =0.42), the temporal correlation is strong (R=0.95). The simulated and observed HCHO seasonal modulations in Europe are, respectively 60% and 62%. The model–satellite discrepancies are prominent in Europe and W-USA during summer and autumn. However, the model–satellite agreement is strong during the winter in these regions. During winter, anthropogenic VOC emissions drive the HCHO variability in these regions (Luecken et a., 2018; Pozzani et al., 2002). Therefore, the simulated contribution of anthropogenic sources to the HCHO abundances during winter in these regions is reasonable.

(c) Central, Northern, and Southern Africa

Over the African regions, the spatial correlation varies between 0.56 and 0.89. The African continent is the single largest biomass-burning emission source (Roberts et al., 2009). CHASER has well-reproduced Central African (C-Africa) HCHO seasonality, with a peak of 2×10^{16} molecules cm^{-2} in September. The observed and simulated amplitude of the HCHO seasonality in C-Africa are, respectively, 61 and 55%. The mean simulated and observed HCHO abundances in the N-Africa biomass burning season are ~1.06×10^{16} molecules cm^{-2}, consistent with the GOME-2 and SCIAMACHY observations (De Smedt et al., 2008). Figure S4 (Supplementary Information) shows the seasonal fire radiative power (FRP) cycle over C- and North Africa in 2019. FRP, a measure of outgoing radiant heat from fires, is considered a tracer

of changes in atmospheric trace constituents related to pyrogenic emissions (Hoque et al., 2018a). The observed and simulated enhanced HCHO columns in both regions are congruent with the high FRP values, manifesting the contribution of biomass burning to the HCHO abundances.

Over Southern Africa, elevated TROPOMI HCHO columns are consistent with GOME-2 and SCIAMACHY observations (De Smedt et al., 2008. The observed peaks in HCHO columns and FRP values are consistent and thus can be attributed to biomass burning. The lower CHASER columns in Southern Africa are likely attributable to underestimated pyrogenic emissions. TROPOMI and CHASER have captured the shift in biomass-burning seasons from northern to southern Africa, which agrees well with earlier observations (i.e., GOME-2, SCIAMACHY). The observed amplitude of the HCHO seasonal cycle in South and North Africa is 46%, signifying an almost two-fold increase in HCHO abundances during the biomass-burning season. Earlier studies (e.g., De Smedt et al., 2008; Muller et al., 2008) found that such a feature (increment by a factor of 2) exists only in the Southern African region. This likely indicates an increase in fire intensity in Northern Africa.

(d) South America

CHASER showed moderate skill in reproducing the observed HCHO spatial distribution in South America (S-America; r = 0.56). However, the seasonal variation in the HCHO columns is strongly correlated (R = 0.96). The MBE and RMSE in the South American continent are, respectively, 2.34×10^{15} and 2.385×10^{15} molecules cm^{-2}. The enhanced HCHO columns during the South American biomass burning season are well reflected in the datasets. They show a distinctive seasonal cycle. The observed and simulated mean HCHO columns from August through October are ~1.5×10^{16} molecules cm^{-2}, higher than the HCHO columns during the North African biomass burning season. CHASER estimated 46% seasonal modulation in the HCHO abundances, whereas the observed modulation is 59%. The model overestimates the HCHO columns in S-America, similarly to C-Africa and N-Africa, probably because of the uncertainties in biogenic emission inventories.

(e) India

CHASER well reproduced the observed HCHO spatial distribution in India (r =0.91), with MBE and RMSE of -1.0×10^{15} and 1.45×10^{15} molecules cm^{-2}. Both datasets also show good agreement regarding the temporal variation (R=0.77). However, seasonal modulation of 30% manifests a less-prominent seasonality in HCHO abundances in India. India has a diverse landscape, including major forests over the east, northeast, and southwest regions and desserts in north western India (Surl et al., 2018). The Indo-Gangetic Plain (IGP) stretches from Eastern Pakistan to Bangladesh and is a major agricultural region in India (Kuttippurath et al., 2022). Considering the diverse Indian landscape, the model satellite comparison over three regions in India (IGP, east India, and South India) is shown in Fig.2.

The model has shown good skill in reproducing the observed HCHO spatial variation in the IGP (Indo-Gangetic Plain) region (r = 0.91). However, the temporal correlation is moderate (R=0.44). Several field studies (e.g., Hoque et al., 2018b) have reported biomass-burning influences during spring and autumn in IGP, explaining the elevated observed HCHO columns. HCHO seasonal variation during January–June is consistent in both datasets, with an R-value of 0.78. The mean observed and modeled HCHO abundances during spring in IGP are, respectively 1.19×10^{16} and 8.72×10^{15} molecules cm^{-2}. However, the model was unable to reproduce the autumn-time biomass-burning events, thereby reducing the overall R-value in the IGP region. CHASER underestimates winter HCHO columns in the IGP region. Liquid petroleum gas (LPG) usage, evaporative fuels, and garbage burning contribute significantly to winter NMVOC levels in Delhi and Mohali (Kumar et al., 2021). Although NMVOC emission from these sources are considered in the simulations, it is likely underestimated for the IGP region.

Over East India, both the spatial (r = 0.86) and temporal (R = 0.72) agreement between TROPOMI and CHASER HCHO are strong. The observed and modeled amplitudes of the HCHO seasonal cycle are 40%. Both datasets show enhanced HCHO levels during spring., consistent with high isoprene concentrations (Fig.) Biogenic emissions are the main driver of the HCHO levels in East India, however, emissions from mines are also potential sources of NO_x and VOCs (Kuttippurath et al., 2022).

Similarly, CHASER has shown a strong capability for reproducing the HCHO spatial distribution (r=0.96) in south India (S-India). However, the temporal correlation is low. The mean observed and simulated HCHO abundances are, respectively, 4.68×10^{15} and 5.03×10^{15} molecules cm^{-2}. The HCHO seasonality in S-India is less prominent compared to the other two regions. The coordinates bounds defined for S-India in this study compromises a large portion of the southern coastal region, which experiences a tropical maritime climate with limited seasonal variations in temperature (Surl et al., 2018). Such a feature can potentially lead to a less prominent HCHO seasonality in S-India.

(f) Southeast Asia

In Southeast Asia (SE-Asia), the r-value is 0.71. The MBE and RMSE are respectively -0.77×10^{15} and 1.2×10^{15} molecules cm^{-2}. During the dry season (January–April), prominent biomass burning occurs in this region in many countries (e.g., Thailand, Malaysia, Indonesia, Cambodia). Such fire events degrade local air quality and cause transboundary pollution (Hoque et al., 2018; Kahn et al., 2016). TROPOMI and CHASER have well-captured the pyrogenic emissions-led enhanced HCHO levels. The simulated and observed mean dry season HCHO columns are, respectively, 1.07×10^{16} and 1.35×10^{16} molecules cm^{-2}. The observed and simulated amplitude of the seasonal cycle are, respectively, 48 and 60%. CHASER-reproduced columns during the dry season are underestimated. Potential reasons for such discrepancies are discussed in section 3.3.

(g) Remote Pacific region

The datasets correlate strongly over the remote Pacific region, representing the background condition. No prominent seasonal variation is observed in this region, which has been well simulated by CHASER. The simulated and observed background HCHO column is 2.86×10^{15} molecules cm^{-2}.

3.2 Comparison over countries with large forested areas

Figure 3 shows the observed and simulated HCHO columns over countries where large forested areas are located. The definition of the countries is adopted from the work of Opacka et al., (2021). The statistics presented in Table 4, include regions with high and low biogenic activities. The aim of this section is to compare the overall biogenic emissions in the defined regions with literature values and assess its impact on the model performance. The statistics in Table 4 will certainly vary if regions with high biogenic emissions are considered only.

Over China, CHASER correlates strongly with TROPOMI (r = 0.92), with MBE of -3×10^{15} molecules cm^{-2}. The lowest differences between the datasets are observed primarily in the southeastern and western parts of China. Shanghai, Nanjing, and Guangzhou megacities are located in southeastern China. Consequently, CHASER has demonstrated good skills in the areas encompassed by multiple megacities. The annual isoprene emission for China in CHASER is 34 TgC/yr: higher than that of Opacka et al. (2021) (9.5–23 TgC/yr).

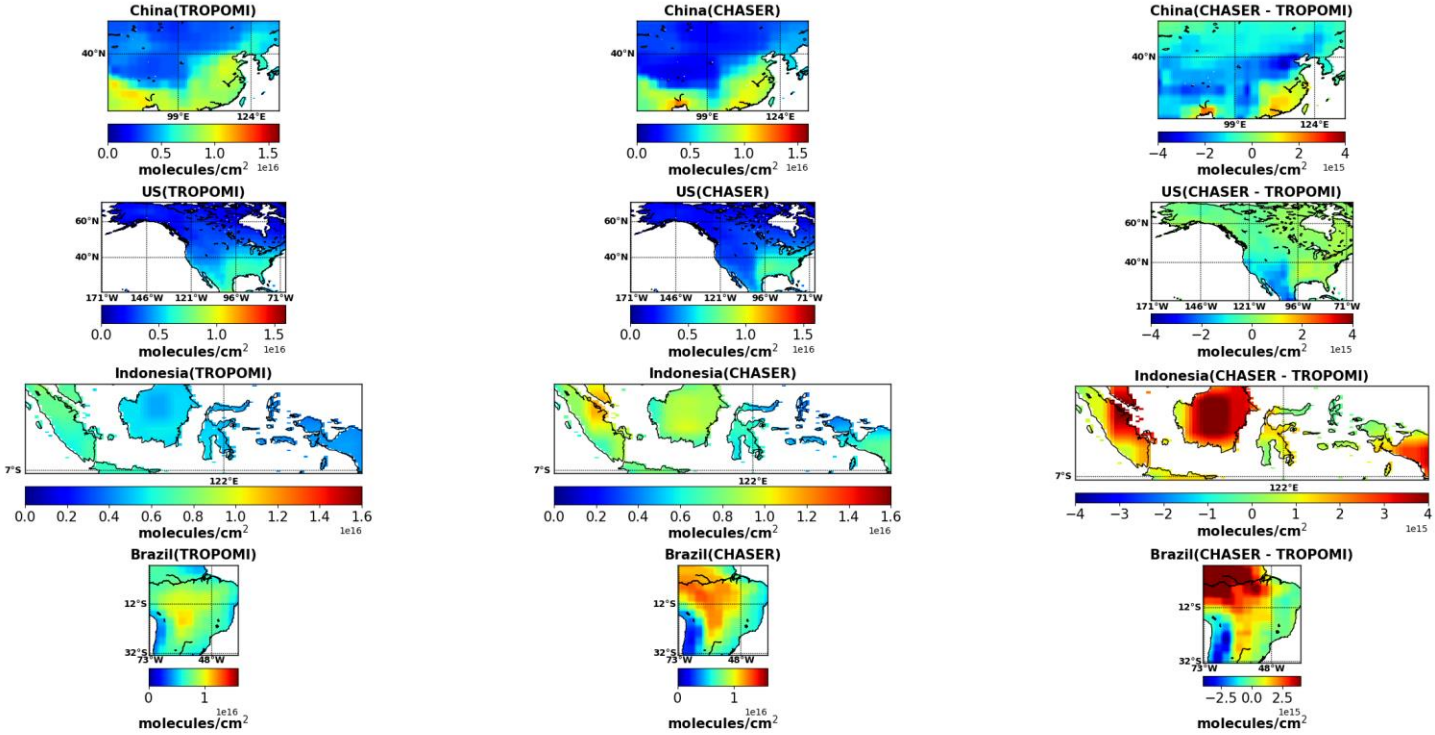

Figure 3: Two-year (2019 and 2020) mean CHASER (first column) and TROPOMI (second column) HCHO columns ($\times 10^{16}$ molecules cm^{-2} cm^{-2}) in China (18.19–53.45°N, 73.67–135.02°E), United States (18.91–45°N, 66–171°W), Indonesia (10°S–6°N, 95–142°E), and Brazil (33°S – 5.24°N, 34–73°W). The differences between the datasets are presented in the third column. Only the coincident dates among the datasets are used to calculate the annual mean data.

Table 4: Comparison of two-year mean HCHO ($\times 10^{15}$ molecules cm^{-2}) column between TROPOMI and CHASER over countries with large forested areas. The coordinate bounds of the regions are adapted from Opacka et al. (2020). Correlation signifies the spatial agreement between CHASER and TROPOMI. The unit of MBE is $\times 10^{15}$ molecules cm^{-2}

Region	**Correlation (model vs. TROPOMI)**	**MBE (model–TROPOMI)**
China	0.92	-0.84
US	0.93	-0.05
Indonesia	0.81	1.05
Brazil	0.84	1.06

CHASER has shown excellent skill in reproducing TROPOMI observations over the US. Along with high *r*-values, the simulated magnitude of the HCHO columns is consistent with observations throughout the whole region. Consequently, the bias between the datasets for the US is 2%. In CHASER, annual isoprene emissions in the US and the southeastern US are 22 and 7.8 TgC/yr, respectively. Such values are within the ranges reported by Stavrakou et al. (2015) and Opacka et al. (2021).

The MBE between TROPOMI and CHASER in Indonesia is 1.05×10^{15} molecules cm^{-2}. The *r*-value is 0.81. Indonesia's annual mean TROPOMI and CHASER HCHO abundance are 5.06×10^{15} and 6.15×10^{15} molecules cm^{-2}. The most significant differences between the datasets (4×10^{15} molecules cm^{-2}) are observed for Sumatra, Borneo, and Sulawesi islands. Annual isoprene emissions in Indonesia used in the CHASER simulations are 42 TgC/yr. Indonesian isoprene emissions vary between 25.5 to 32 TgC/yr depending on the land-use change (Opacka et al., 2021). Top-down estimates based on OMI and GOME-

2 observations are ~11 TgC/yr (Stavrakou et al., 2015). However, the 11 TgC/yr emissions are half of the top-down estimates based on SCIAMACHY observations. Consequently, isoprene emissions in Indonesia remain largely uncertain. However, CHASER estimates with the VISIT emissions are higher than the values reported in the literature, likely leading to the model overestimation in Indonesia.

CHASER overestimates the HCHO columns over the Amazonia, mostly in northern Brazil. Fig. shows the observed and simulated seasonal HCHO variation over Brazil. Although the model well reproduced the temporal variability, the magnitude has been overestimated. This indicates that emission uncertainties are more prominent than uncertainties related to chemical mechanism for this region. In CHASER, annual isoprene emissions over Amazonia are 67 Tg/yr, which is consistent with the OMI-based top-down estimates of 70 Tg/yr (Stavrakou et al., 2015). However, deforestation affect the VOC emissions in the Amazon (Yáñez-Serrano et al., 2020). Massive deforestation in the Amazon occurred between 1985 and 2020, changing 11% of the Amazonian biome (Cabarello et al., 2022). Depending on the land use and land cover change(LULCC), isoprene emissions in Brazil can vary between 79. And 106.5 Tg/yr (Opacka et al., 2021). Moreover, although biogenic VOC modelling in the amazon has improved, VOC dynamics in the changing Amazonian biome is not well understood (Salzar et al., 2018; Taylor et al., 2018). Therefore, updated biogenic VOC and LULCC inventories can potentially improve the model performance in Brazil.

In addition, CHASER isoprene emission estimates for Europe and Russia are, respectively, 17 and 15 TgC/yr, which are comparable to values reported in the literature (e.g., Guenther et al., 2006; Sinderolova et al., 2022).

The discussion is based on isoprene emissions because isoprene is the dominant biogenic VOC (BVOC). Although not included in the current discussion, the chemical yield of HCHO from the oxidation of other BVOCs might also be a source of model uncertainty.

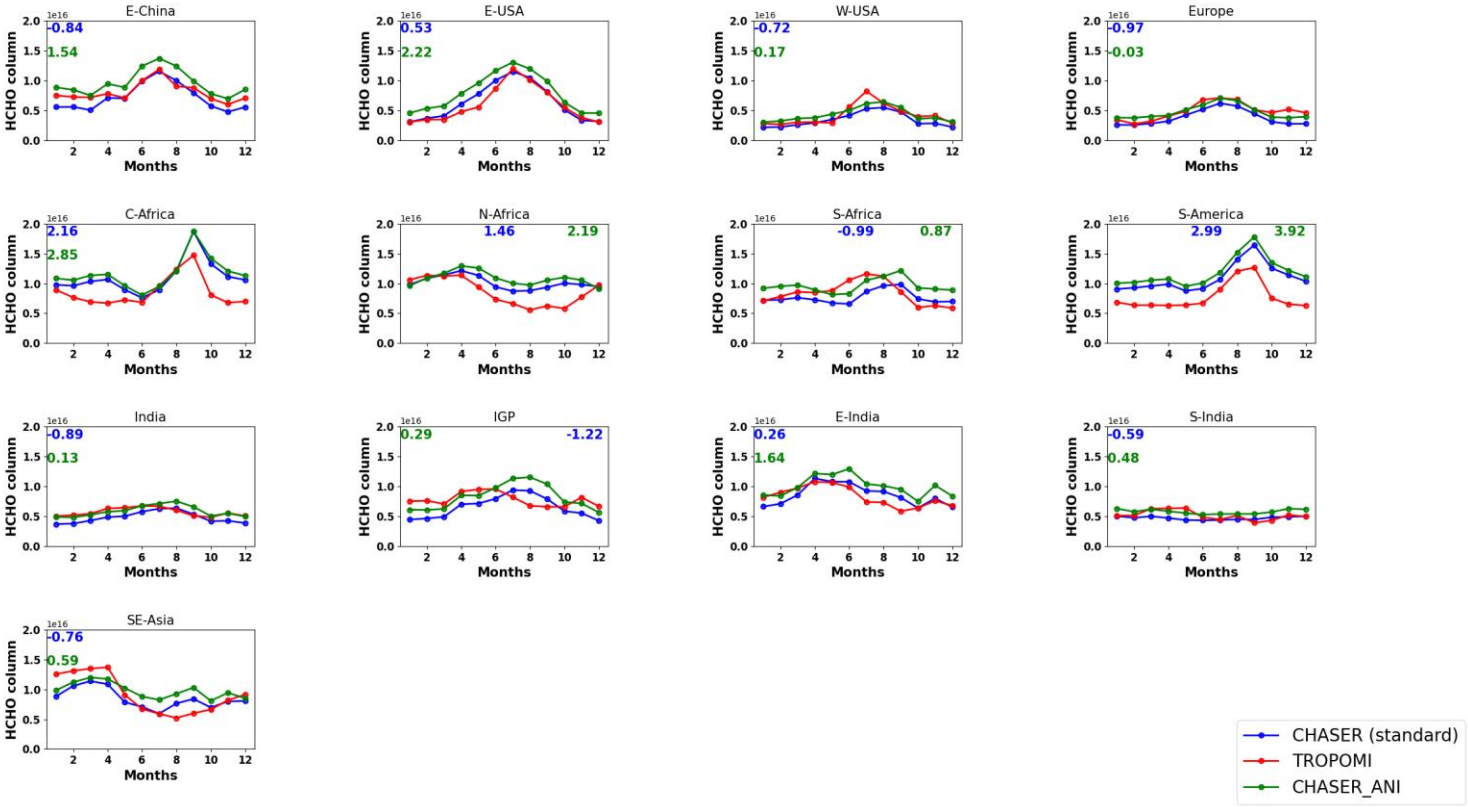

Figure 5: Seasonal variation of HCHO ($\times 10^{16}$ molecules cm^{-2}) in the selected regions, as inferred from standard simulations (blue), TROPOMI observations (red), and ANI estimate (green). Anthropogenic VOC emissions are increased threefold in the ANI simulations. The blue numbers denote MBE between the TROPOMI and CHASER HCHO columns. The MBE between ANI and TROPOMI columns are shown as green. The coordinate bounds of the regions are similar to those in Fig. 2.

3.3 Uncertainties related to the anthropogenic emissions

In addition to background uncertainties, uncertainties in anthropogenic emissions can also be crucially important. Figure 5 presents a comparison of the TROPOMI HCHO columns and ANI simulations in 2019. The anthropogenic VOC emissions are increased threefold in the ANI simulations. Standard simulation estimates for 2019 are also shown. The comparison statistics are provided in Table 5.

Over E-China, ANI winter estimates show better agreement with TROPOMI than with CHASER. Similarly, over the Indian region, ANI estimates reduce the winter-time MBE and RMSE. In India and China, the contribution of anthropogenic emissions to the NMVOC levels is more significant during the winter (Kumar et al., 2021; Liu et al., 2021). Thus, the ANI simulations improve the anthropogenic contribution in these regions.

The increased anthropogenic VOC emissions do not affect the HCHO columns in C-Africa, N-Africa, S-Africa, or in South America, E-USA or Europe, which indicates that the anthropogenic VOC emission estimates in these regions used for the standard simulations are reasonable.

ANI estimates during the dry season in SE-Asia are similar to the standard simulation values, indicating a small effect of anthropogenic emission uncertainties. However, when the anthropogenic VOC emissions are increased fivefold (Fig. S5), the dry season HCHO levels overestimate the observations. Space-based observations have provided substantial evidence of increasing anthropogenic VOC emissions in Asian cities (Bauwens et al., 2022). Simulations with updated anthropogenic VOC emissions can likely reduce the discrepancy between CHASER and TROPOMI over Asia.

Table 5: Comparison among regional mean tropospheric HCHO ($\times 10^{16}$ molecules cm^{-2}) columns inferred from TROPOMI observations, standard simulation and ANI estimates. Units of MBE1, MBE2, RMSE1, and RMSE 2 are $\times 10^{15}$ molecules cm^{-2}.

.

Region	MBE1 (Standard–TROPOMI)	MBE2 (ANI–TROPOMI)	RMSE1 (Standard–TROPOMI)	RMSE2(ANI–TROPOMI)
E-China	-0.84	1.54	1.40	1.74
E-USA	0.53	2.22	0.58	2.25
W-USA	-0.72	0.17	0.80	0.43
Europe	-0.97	-0.03	1.17	0.67
C-Africa	2.16	2.85	2.32	2.94
N-Africa	1.46	2.19	1.61	2.30
S-Africa	-0.99	0.87	1.32	1.39
S-America	2.99	3.92	3.41	4.28
India	-0.89	0.13	1.31	1.14
IGP	-1.22	0.29	1.69	2.02
E-India	0.26	1.64	1.22	2.11
S-India	-0.59	0.48	0.69	0.58
SE-Asia	-0.76	0.59	1.16	0.78

3.4 Impacts of NO_x emissions uncertainties on HCHO simulations

Uncertainties in the NO_x emissions can affect the HCHO abundances through the NO_x-HO_x-VOC cycle. Such effects are assessed by comparing simulations with different NO_x inventories with the TROPOMI observations. The CHASER standard, OLNE, and TROPOMI HCHO columns are depicted in Fig. 6. The HTAP_v3 NO_x emission inventory is replaced with the HTAP_v2.2 inventory in the OLNE simulations, without altering the remaining emission inventories. The differences between the two NO_x inventories are – (1) HTAP-v3 inventory considers the changes in NO_x emissions from 2000 to 2018, whereas the temporal coverage of HTAP_v2.2 is 2008 – 2010, and (2) Emissions in HTAP-v3 have a higher sectoral disaggregation (Crippa et al., 2023). The comparison-related statistics are given in Table 6.

On a global scale, HCHO column estimates are mostly unaffected by the changes in the NO_x emission inventories, manifested by the MBE values (Table 6). However, RMSE is 8% lower in the case of standard simulation. OLNE estimates in the higher latitude (>=50ºN) are 5% lower than the standard simulations. Such differences do not affect the model–satellite agreement in these regions.

The standard HCHO columns in India, China, and Southeast Asia are approximately 10–20% lower than the OLNE estimates. In fact, those differences are consistent with changes in the regional OH estimates. This finding implies that the changes in the NO_x emissions estimates have affected the OH and HCHO abundances in these regions. Satellite data assimilation results reported by Miyazaki et al. (2017, 2020) indicate that, since 2008, NO_x emissions in India have increased by 30%, whereas NO_x emissions in China have declined since 2011 (Liu et al., 2016). Despite the observed NO_x emission trend being opposite in these regions, the effects on the HCHO estimates are similar (i.e., lower values of the standard estimate). Over E-China, the standard simulations reduce the absolute annual mean difference between OLNE and TROPOMI of 3×10^{15} molecules cm^{-2} to 1×10^{15} molecules cm^{-2}. The model satellite agreement is unchanged despite differences between the simulation over India and SE-Asia. A similar small effect of the NO_x emission inventory changes is observed from a regional comparison (Fig. S6). Although the regional MBE (simulation–observation) values change, no significant differences in the RMSE values

were found. Therefore, the effect of NO_x emission uncertainties on the HCHO estimates remains unclear. Although the current HCHO estimates are less sensitive to NO_x emission inventories, two potential perspectives require further investigation: (1) The sensitivity should be assessed at higher model resolution. (2) The magnitude of the observed change in the NO_x emissions might be underestimated in the bottom-up inventory.

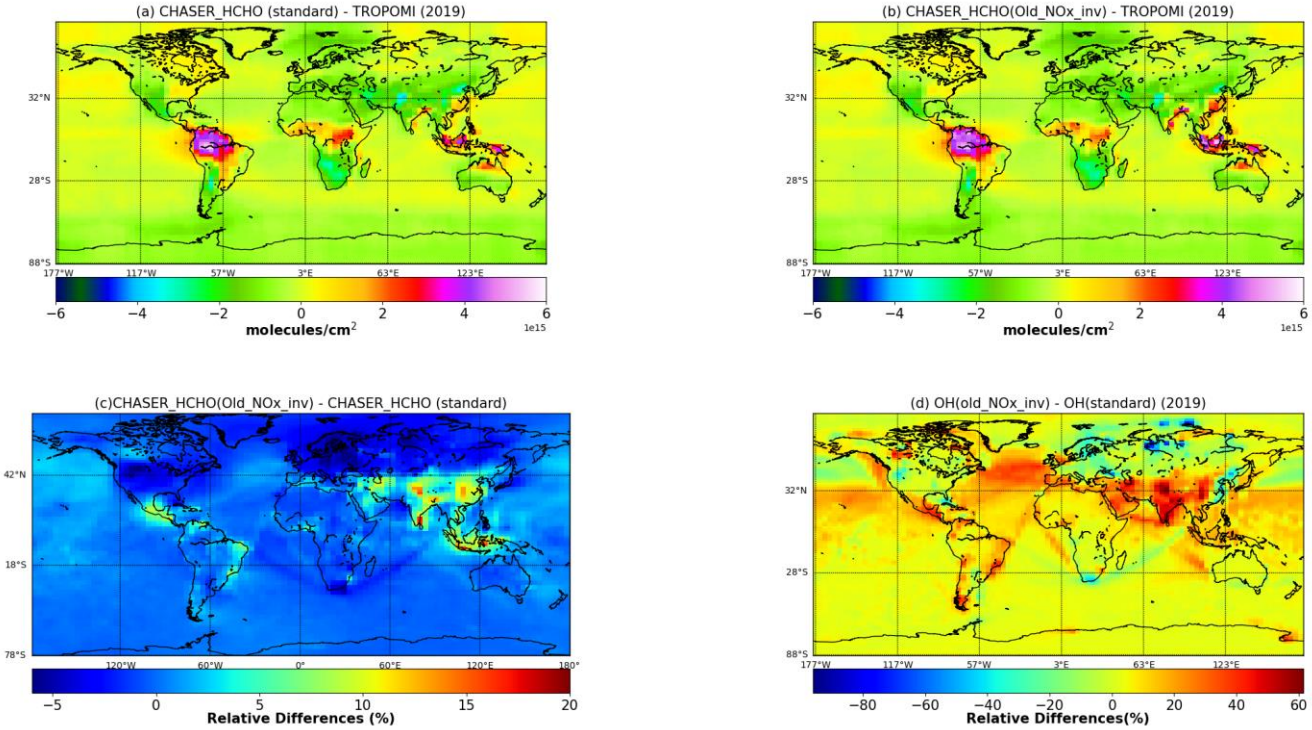

Figure 6: Annual mean HCHO columns ($\times 10^{16}$ molecules cm^{-2}) in 2019, obtained from the (a) standard and (b) OLNE simulations. The HTAP-2008 NOx emission inventory was used instead of the HTAP-2018 inventory for the OLNE simulations (Table 1). The remaining emission inventories are similar in both simulations. (c) Global relative differences between the two HCHO simulations (OLNE–Standard). (d) Relative differences (global) between two OH (OLNE–Standard) simulations. The standard and OLNE OH simulation settings are similar to the description in Table 1. OH and HCHO simulations were obtained simultaneously.

590 **Table 6:** Statistical comparison among regional mean tropospheric HCHO (× 10^{16} molecules cm^{-2})
591 columns inferred from TROPOMI observations, standard simulation, and OLNE estimates. Units of
592 MBE1, MBE2, RMSE1, and RMSE2 are × 10^{15} molecules cm^{-2}.

Region	**MBE1 (Standard–TROPOMI)**	**MBE2 (OLNE–TROPOMI)**	**RMSE1 (Standard–TROPOMI)**	**RMSE2 (OLNE–TROPOMI)**
Global	-0.23	-0.22	0.75	0.81
E-China	-0.84	-0.24	1.40	1.24
E-USA	0.53	0.39	0.58	0.44
W-USA	-0.72	-0.82	0.80	0.89
Europe	-0.97	-0.99	1.17	1.15
C-Africa	2.16	2.23	2.32	2.40
N-Africa	1.46	1.52	1.61	1.69
S-Africa	-0.99	-1.03	1.32	1.34
S-America	2.99	3.05	3.41	3.45
India	-0.89	-0.61	1.31	1.36
IGP	-1.22	-0.57	1.69	1.67

E-India	0.26	1.01	1.22	1.89
S-India	-0.59	-0.44	0.69	0.62
SE-Asia	-0.76	-0.32	1.16	1.21

3.5 Comparison among CHASER, TROPOMI, and OMI

TROPOMI was able to achieve improved precision of HCHO columns at shorter timescales (De Smedt et al., 2021). The effect of such features on the comparison results is evaluated in this section. The method of De Smedt et al., (2021) has been adopted to minimize the effect of different cloud retrieval algorithm used for OMI and TROPOMI retrievals. Figure S7 shows the global distribution mean HCHO columns obtained from TROPOMI and OMI retrievals and CHASER simulations in 2019 during the TROPOMI overpass time (13:30). Only the coincident dates among the three datasets are shown. Global and regional comparison statistics are presented in Table 7.

The spatial correlation between OMI and CHASER is 0.89. OMI retrievals are positively biased by 7% compared to CHASER. A similar bias is also observed between TROPOMI and CHASER. Despite similar MBE values, TROPOMI reduces the global RMSE by 20%. Monthly MBE and RMSE values between OMI and CHASER are higher than those of TROPOMI and exhibit no seasonality (Table S2). The highest absolute differences between the model and OMI retrievals are observed in Amazonia in Brazil, and in C-Africa and SE-Asia. The magnitudes of differences between the model and observation in these regions are similar for both sensors. Despite the improved resolution, TROPOMI and OMI show equivalent biases in regions with high HCHO levels (De Smedt et al., 2021). A regional comparison among the three datasets is portrayed in Fig. 7. The red (TROPOMI–CHASER) and green (OMI–CHASER) numbers are the respective MBE values.

Table 7. Comparison of global mean HCHO columns between satellite observations (TROPOMI and OMI) and standard CHASER simulations. Units of MBE and RMSE are $\times 10^{16}$ molecules cm^{-2}.

Region	**MBE1 (Standard–TROPOMI)**	**MBE2 (Standard–OMI)**	**RMSE1 (Standard–TROPOMI)**	**RMSE2 (Standard–OMI)**	***r*-value (CHASER vs. TROPOMI)**	***r*-value (CHASER vs. TROPOMI)**
Global	-0.23	-0.24	0.77	0.99	0.93	0.89
E-China	-0.84	-2.54	1.40	3.03	0.56	0.17
E-USA	0.53	-1.02	0.58	1.12	0.92	0.86
W-USA	-0.72	-2.09	0.80	2.17	0.83	0.64
Europe	-0.97	-1.6	1.17	1.95	0.50	0.27
C-Africa	2.16	1.34	2.32	1.50	0.79	0.88
N-Africa	1.46	1.42	1.61	1.59	0.81	0.79
S-Africa	-0.99	-2.59	1.32	2.75	0.86	0.84
S-America	2.99	2..02	3.41	2.61	0.47	0.56
India	-0.89	1.67	1.31	2.26	0.92	0.80
IGP	-1.22	-2.85	1.69	3.19	0.91	0.84

E-India	0.26	-0.05	1.22	1.34	0.82	0.76
S-India	-0.59	-0.16	0.69	0.41	0.96	0.97
SE-Asia	-0.76	-0.83	1.16	1.14	0.78	0.86

Over E-China, the monthly mean TROPOMI columns are ~22% lower than those of OMI, reducing the RMSE by 53%. The simulated spatial distribution shows better congruence with the new observations. Actually, TROPOMI improved summer model–satellite agreement considerably. The magnitude of the seasonal modulation in the three datasets is 50%. Both sensors show that winter HCHO levels in E-China are ~8×10^{15} molecules cm^{-2}.

Over E-USA, the *r*-value between CHASER and OMI is 0.86. CHASER columns are underestimated compared to OMI, with MBE and RMSE of -1.0×10^{15} and 1.1×10^{15} molecules cm^{-2}. TROPOMI reduced the model–satellite RMSE by 50% and improved the *r*-value by 6%. The most significant improvements were observed during the summer and autumn.

Over the W-USA, TROPOMI retrievals are 26% lower than OMI observations, reducing the model–satellite RMSE by 63%. The spatial correlation between OMI and CHASER is moderate, whereas CHASER and TROPOMI correlate strongly. The simulated and TROPOMI wintertime columns are ~30% lower than OMI. However, the observed peak in HCHO seasonality in July is consistent in the observational datasets.

OMI and TROPOMI HCHO observations over Europe are consistent. The seasonal cycle amplitude inferred from both sensors is 60%. The simulated spatial distribution shows better agreement with the TROPOMI observations, manifesting the effects of improved resolution.

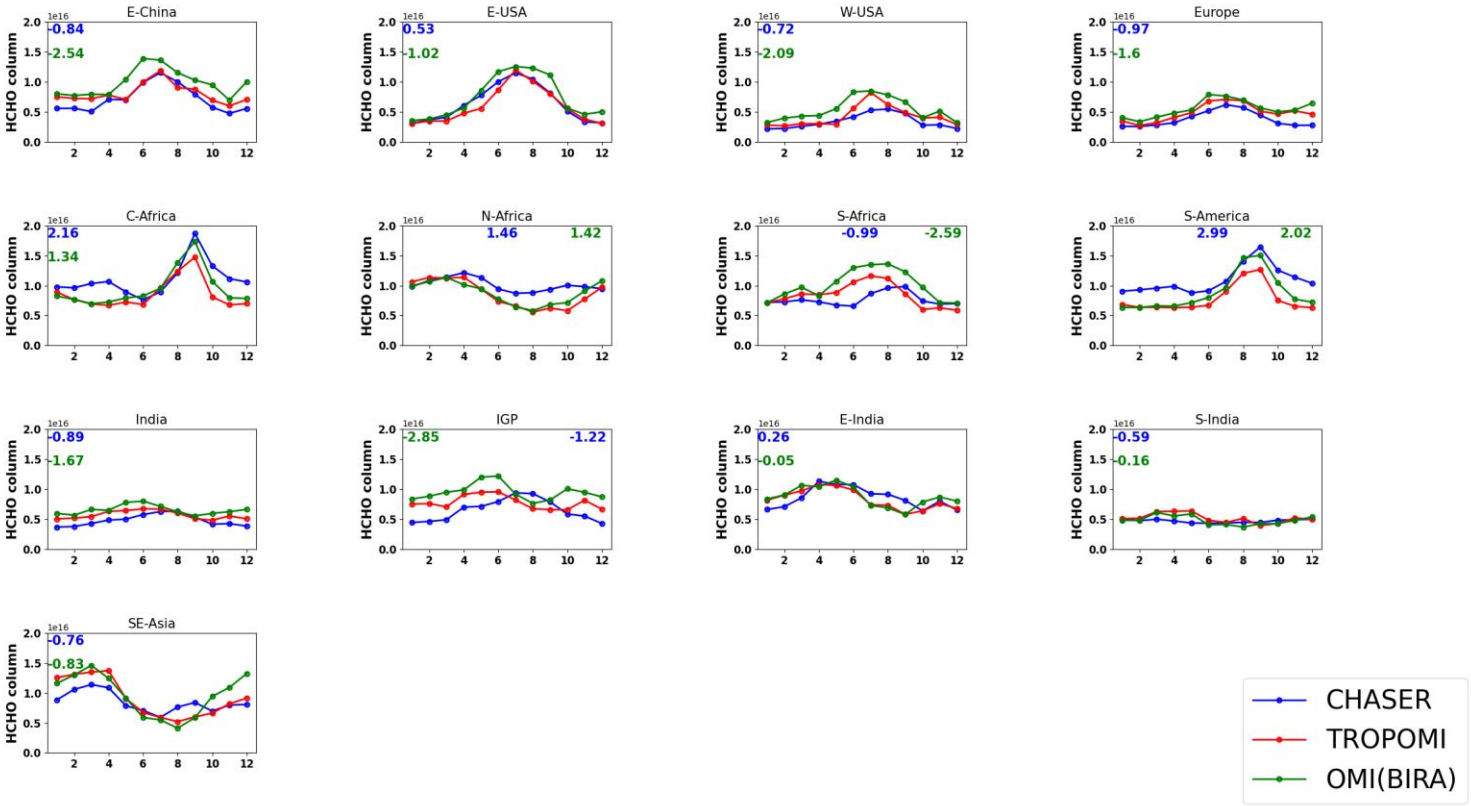

Figure 7: Seasonal variation of HCHO ($\times 10^{16}$ molecules cm^{-2}) inferred from TROPOMI (red curve) and OMI (orange curve) retrievals and standard CHASER (blue curves) simulations. The region definitions are shown in Fig. 2. The blue numbers signify the MBE between TROPOMI and CHASER, whereas the green numbers represent the MBE between CHASER and OMI. Coincident dates among the datasets are used to calculate the monthly mean data.

Over C-Africa, the RMSE value between CHASER and OMI is ~35% lower than that of TROPOMI. CHASER estimates agree better with the OMI observations, with a consistent peak of 2×10^{16} molecules cm^{-2} in September and an *r*-value of 0.88. Compared to OMI, TROPOMI values are biased by 18% on

652 the lower side. Annual mean TROPOMI columns in C-Africa are 8×10^{15} molecules cm^{-2}, which is 20
653 and 9% lower, respectively, than the CHASER and OMI columns.
654
655
656 Over N-Africa, OMI retrievals are moderately correlated with CHASER. The amplitude of seasonal
657 modulation inferred from CHASER, TROPOMI, and OMI are, respectively, 48, 62, and 66%. The RMSE
658 and MBE between OMI and CHASER are, respectively, 1.41×10^{15} and 1.59×10^{15} molecules cm^{-2}. OMI
659 retrievals are approximately 13% higher than TROPOMI. Simulated North African HCHO columns show
660 better consistency with the observations during the biomass-burning season.
661
662 Over southern Africa, OMI HCHO columns are biased respectively by 32 and 25% on the higher side
663 compared to TROPOMI and CHASER. The simulated seasonal variabilities and spatial distribution of
664 HCHO show more relevance to TROPOMI than to OMI.
665
666 Over South America, the simulated peak (1.6×10^{16} molecules cm^{-2}) in the HCHO seasonality shows
667 strong congruence with the OMI observations. Despite such consistency, simulated values are higher than
668 OMI retrievals, with MBE and RMSE of $\sim 2 \times 10^{15}$ molecules cm^{-2}. Observations and simulations show
669 that the peak HCHO abundances can vary between $1.0 \times 10^{16} - 1.8 \times 10^{16}$ molecules cm^{-2} in September.
670 Although the *r*-value between OMI and CHASER is higher than that of TROPOMI, the model's capability
671 to replicate the observed spatial distribution was limited. OMI HCHO columns are positively biased by
672 30% compared to TROPOMI, thereby reducing the model–satellite RMSE by 23%.
673
674 Over India, CHASER HCHO columns are negatively biased by 15 and 31%, respectively, compared to
675 TROPOMI and OMI observations. Although TROPOMI minimized the model–satellite bias, seasonal
676 discrepancies between the model and observations prevail. Over the IGP region, OMI HCHO retrievals
677 are biased respectively by 24% and 36% on the higher side, compared to TROPOMI and CHASER. Both
678 sensors captured a similar HCHO seasonality in the IGP, with a modulation of 49%. Although CHASER

was unable to reproduce the seasonality, the simulated modulation is 48%. The bias between the model and observations is 4% in E-India and S-India. Simulated HCHO spatial variation strongly correlates with both the observation datasets (*r*-value of ~0.85). The amplitude of the seasonal modulation in E-India inferred from CHASER, TROPOMI, and OMI is ~40%.

Over Southeast Asia, CHASER columns are negatively biased by 7 and 19%, respectively, compared to TROPOMI and OMI columns. Despite lower biases, the model–satellite discrepancies during the dry season are similar for both datasets. A few reasons for the CHASER underestimation in SE-Asia during the dry season have been discussed in section 3.2. In addition, assumptions and uncertainties in the retrieval could also potentially engender such model satellite discrepancy. Figure S8 compares CHASER and OMI SOA (González et al., 2016) products. The data selection criterion is similar to the description presented in Section 2. The comparison statistics are given in Table S4. CHASER columns during the dry seasons in SE-Asia show excellent agreement with the OMI SOA retrievals. OMI SOA values during the dry season are negatively biased by 7% compared to TROPOMI observations. The MBE between CHASER and SOA product is 0.04×10^{15} molecules cm^{-2}. Based on comparison with OMI SOA products, the model performance during the dry season can be regarded as excellent. The emission estimates for SE-Asia in CHASER can be regarded as reasonable, too.

Similarly, in E-China, the OMI SOA product reduces the bias between the model and observations by 11%. The simulated wintertime columns are consistent with the SOA estimates, but underestimated compared to TROPOMI. The ANI estimates for this region are higher than the SOA product, manifesting that the anthropogenic emissions in CHASER for this region are rational. Therefore, uncertainties related to the retrieval procedure can also significantly affect the comparison results on a regional scale.

Comparison between CHASER and OMI BIRA HCHO products shows differences from the results of Hoque et al. (2022), where the simulation and observations for 2017 were used. The simulations in both studies are similar. However, the OMI data in the earlier study are systematically higher, mainly causing

the statistically significant differences found between the study results. A detailed investigation of the reasons will be addressed in a separate work.

3.6 Validation using MAX-DOAS observations

3.6.1 Seasonal Variation

CHASER columns are compared with ground-based MAX-DOAS observations in Phimai, Chiba, and Kasuga in Fig. 8. Coincident TROPOMI observations over the sites are used for comparative discussion. The TROPOMI AK applied standard and OLNE simulations are used. MAX-DOAS observations between 12:00 and 15:00 were averaged to estimate the monthly mean columns. Only the common dates among the three datasets were compared. De Smedt et al. (2021) compared the TROPOMI and A-SKY MAX-DOAS datasets in Phimai and Chiba. Because, the model-ground-based comparison is the primary focus of this comparison effort, we do not consider the differences in the vertical sensitivity of TROPOMI and MAX-DOAS. Thus, the statistics will differ from De Smedt et al., (2021).

In Phimai, standard CHASER HCHO seasonality correlates strongly (R=0.71) with the MAX-DOAS observations; it is underestimated by 39%. However, the bias between the standard model estimates and TROPOMI observations is 4%. Despite strong correlation, TROPOMI observations are negatively biased by 37% compared to the MAX-DOAS (R=0.84). Such underestimation might be related to the coarse binning of the satellite data. Using a finer bin, De Smedt (2021) reported a negative bias of 23% in Phimai.

Biomass burning-led enhancements during the dry season (January–April) are well reflected in the simulations. During the wet season, MAX-DOAS, TROPOMI, and standard CHASER HCHO columns are mostly lower than 1×10^{16} molecules cm^{-2}. The simulated standard HCHO peak in March is consistent with the satellite observation, whereas MAX-DOAS observation shows a peak during February. During the dry seasons of 2015 and 2016, the HCHO peak was observed in March (e.g. Hoque et al., 2018).

Consequently, such a shift in the HCHO peak might be related to fire numbers and fire radiative power changes (Hoque et al., 2022).

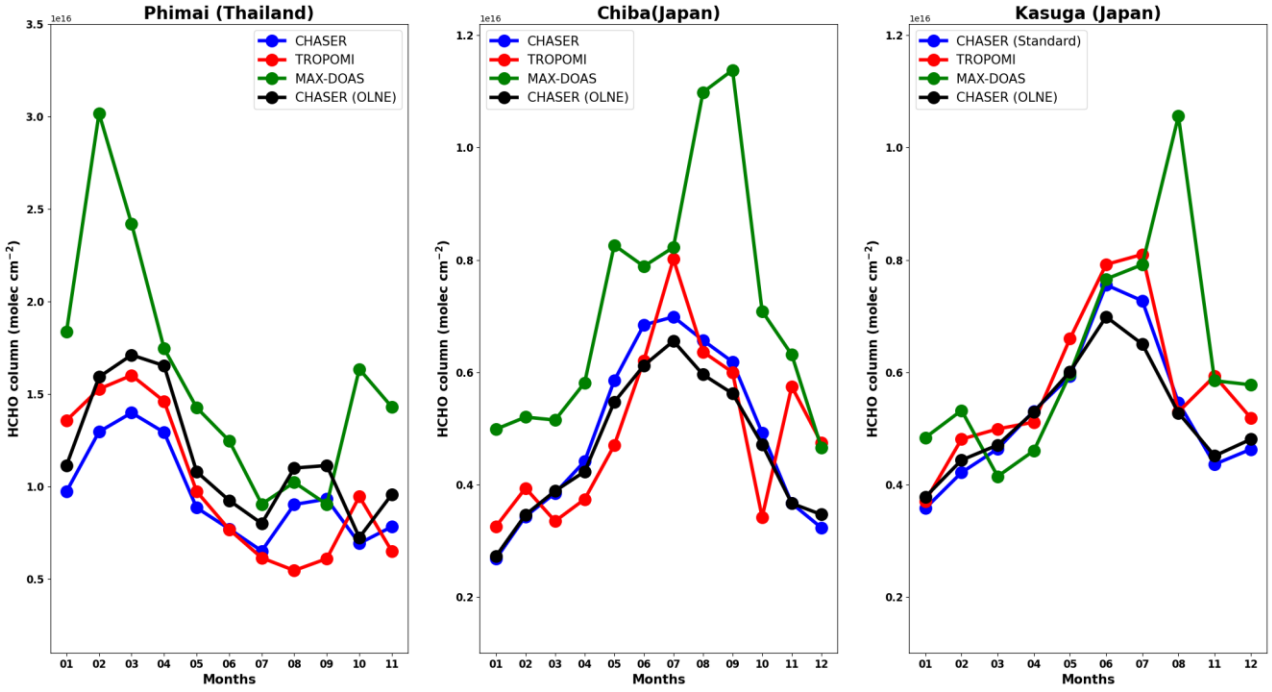

Figure 8: Seasonal variations in HCHO (× 10^{16} molecules cm^{-2} cm^{-2}) columns inferred from satellite retrievals (red), model simulations (blue and black), and ground-based MAX-DOAS observations (green) in Phimai (Thailand), Chiba (Japan), and Kasuga (Japan). MAX-DOAS observations and CHASER simulations during 12:00–14:00 LT were selected for comparison. Common dates among the datasets are used to calculate the monthly mean statistics. The blue and black curves respectively signify the standard and OLNE simulations. TROPOMI AKs have been applied to both simulations. The settings of the simulations are provided in Table 1.

The bias between OLNE and MAX-DOAS observations is 27%. OLNE estimates agree better with the TROPOMI observations during the dry season. However, the overall bias (13%) between the model and satellite observations is higher in the case of OLNE simulations.

At Chiba, the simulated HCHO seasonality correlates strongly with the MAX-DOAS retrievals (R=0.81) and is negatively biased by ~31%. The amplitudes of seasonality inferred from the simulations, MAX-DOAS observations, and TROPOMI retrievals are, respectively, 59, 60, and 34%. The MAX-DOAS, TROPOMI, and CHASER HCHO columns respectively reach peaks in September, July, and June. Similar to Phimai, the HCHO peaks in satellite and ground-based observations differ. One reason might be the differences in spatial representativity. TROPOMI data used for comparison are spatially averaged over 200 km, centering on the Chiba site, whereas the spatial representativity of the MAX-DOAS is approx. 10 km. Moreover, MAX-DOAS observations are most sensitive to altitudes near the surface, whereas satellite sensitivity decreases near the surface. Consequently, the air masses sampled by the instruments at the same local time might be different, leading to inconsistent observation peaks.

At Kasuga, the simulated HCHO levels are strongly correlated with the TROPOMI observations (R = 0.75) and are negatively biased by 35%. Although the correlation between the model and MAX-DOAS retrievals is moderate, the bias between CHASER and MAX_DOAS retrievals is 14%. Therefore, CHASER shows better agreement with MAX-DOAS than with TROPOMI. MAX-DOAS observations exhibit seasonality similar to that of Chiba, with a peak HCHO column during August. Similar to Chiba, the satellite-observed and CHASER peaks are observed during July and June, respectively. Chiba and Kasuga sites are located near the ocean, therefore exhibiting similarity in HCHO variability, which has been well captured in the simulations.

Although the bias between OLNE and standard simulations for Chiba and Kasuga is ~4%, the absolute difference is ~1×10^{15} molecules cm^{-2}. NO_x emissions in Japan have not changed markedly since 2005 (Miyazaki et al., 2017). The differences between the simulations are observed during the summer when isoprene emissions are expected to peak (Hoque et al., 2018a). Because the OH estimates over Japan are

similar for both simulations (Fig. 6(d)), the differences are likely related to the interaction between isoprene and NO_x inventories.

3.6.2 Diurnal and Daily Variations

Figure 9 presents a comparison of the observed and simulated daily and diurnal variations in the surface HCHO vmr. The error bars represent the 1σ standard deviation of the observed mean values. The daily variation comparison entails only the standard simulations.

In Phimai, the daily datasets correlate well, with an *R*-value of 0.67. The slope of the fitted line is 0.37. The observed and simulated daily mean HCHO vmr is ~4 ppbv. CHASER daily mean values are negatively biased by 19% and 11%, respectively, during the dry and wet seasons. The standard diurnal variations at Phimai are also well correlated with the observations (*R*=0.64). The simulated values lie within the standard deviation of the observations. HCHO mixing ratios show a peak (~6 ppbv) at 8:00 LT in both datasets. Noontime (12:00 LT) vmr are approximately 4 ppbv, and hourly HCHO levels vary between 2 and 6 ppbv. The OLNE diurnal values are 20% higher than the standard values. However, the mean absolute difference between the two simulations is 1 ppbv.

The standard simulation reproduced the observed diurnal variations at Chiba, with a temporal correlation of 0.79, higher than at Phimai. Both simulations are biased by 10% on the lower side compared to the observations. No distinctive peak is observed in the diurnal variations. The increasing daytime HCHO levels in Chiba are well reflected in the model runs. The simulated daily mean values in Chiba are negatively biased by 18%, with correlation of 0.40. The slope of the fitted line to the daily mean concentrations is 0.29, lower than at Phimai, suggesting a higher underestimation similar to the total columns (Fig. 9).

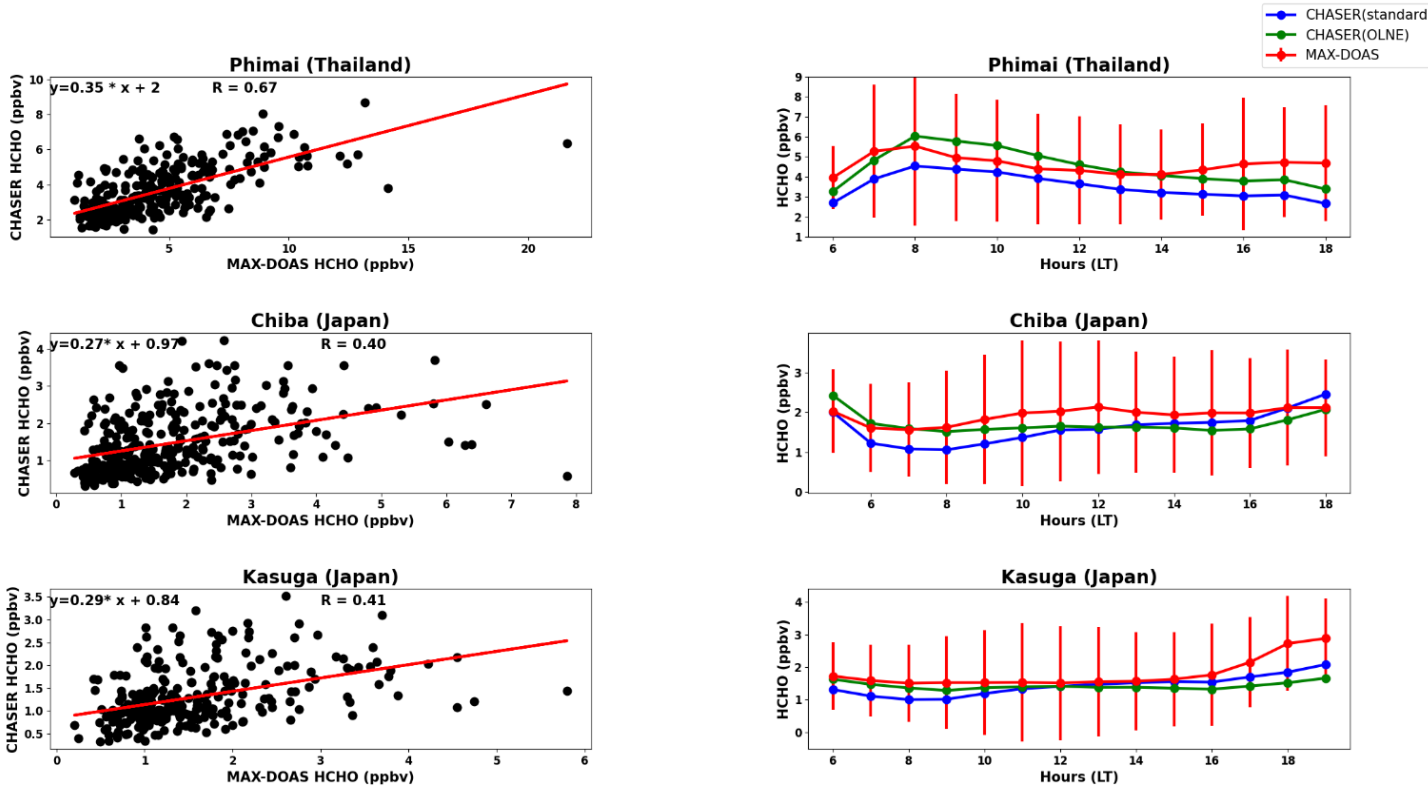

Figure 9: (left panel) Scatter plots show the correlation between the daily mean observed (MAX-DOAS) and simulated HCHO surface mixing ratios at the three sites. The standard simulations are used in the scatter plots. The linear fitted lines are shown in red. (right panel) Diurnal variations in the HCHO mixing ratios at the three sites are inferred from the MAX-DOAS observations and standard (blue) and OLNE (green) simulations. The error bars represent the 1-sigma standard deviation of the mean values estimated from the observations. Observations and simulations at the coincident date and time (local) are selected for comparison.

In Kasuga, modelled diurnal variations correlate strongly (R=0.85) with the observations. The effect of the NO_x inventories on the simulated diurnal variations in Kasuga is not significant. Although Chiba and Kasuga are similar sites, their observed diurnal variations are slightly different. However, the simulated

values in both cases agree with the observed standard deviation. The simulated daily mean values are negatively biased by 20%. The correlation and slope of the fitting are, respectively, 0.39 and 0.29.

3.7 Comparison with ATom-4 flight observations

A comparison between simulated and observed HCHO and isoprene profiles between along the ATom-4 flight path (Fig. S2) is depicted in Fig. 10 (a and c). Only the coincident dates have been included in the comparison.

The simulated HCHO and isoprene profiles agree well with the observations, with an *R*-value of 0.95. Above and below 4 km, CHASER HCHO profiles are positively biased by 29 and

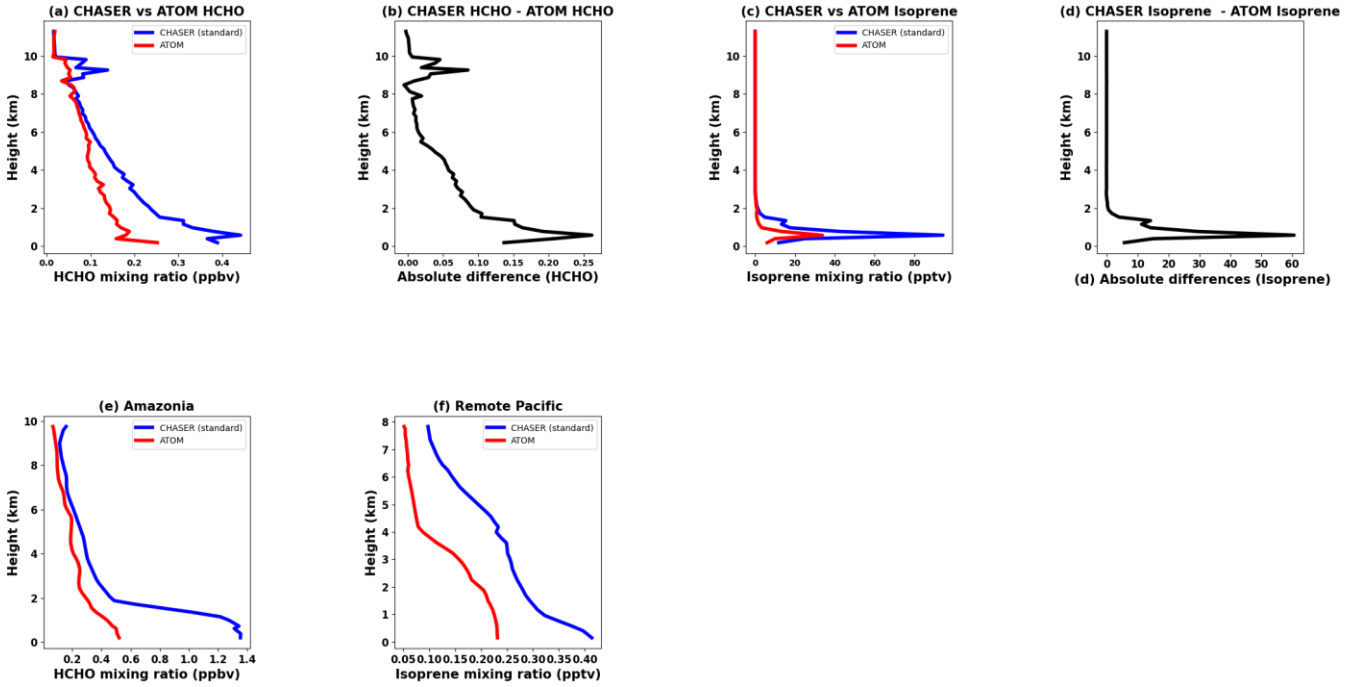

Figure 10: (top panel) Comparison between ATom observed (red) and CHASER simulated (blue) (a) HCHO, and (c) isoprene profiles along the ATom-4 flight path between 20–21 LT (UTC) in 2018. The ATom-4 flight path is depicted in Fig.S4. Standard simulations are used for comparison. Simulations at the time of the ATom observations were selected. Both datasets were averaged within a 0.3 km bin. The relative differences between the observed and simulated (c) HCHO and (d) isoprene profiles are also shown. (bottom panel) Atom-4 observed, and CHASER simulated HCHO profiles over the (e) Amazonia and (f) the Remote Pacific region are compared. Amazonia (10º-40ºS,10ºS-10ºN) represents a densely vegetated region, whereas the remote Pacific region (170º-180ºE, 19º-30ºS) represents the background HCHO conditions. The units of the HCHO and isoprene mixing ratios are, respectively, ppbv and pptv.

72%, respectively, compared to ATom-4 HCHO levels. The absolute difference in the isoprene profiles around 1 km is 60 pptv, which strongly correlates with the difference in the HCHO profile below 2km. This finding signifies that overestimated CHASER isoprene mixing ratios induce a positive bias in the HCHO estimates. Despite non-significant isoprene mixing ratios at altitudes greater than 2 km, both datasets show considerable HCHO levels above 2 km. Zhao et al. (2022) reported a similar finding and attributed enhanced CH_4 oxidation in the presence of water vapor to the HCHO mixing ratios above 2 km. Therefore, despite the differences in the magnitude, CHASER has shown good skills in reproducing the VOC profiles.

The potential reason for the higher HCHO simulated values below 2 km could be CHASER's overestimated HCHO mixing ratios over South America, mainly over the Amazon (Fig 2). Figure 10(e and f) depicts the observed and simulated HCHO profiles over the Amazon (10º-40ºS,10ºS-10ºN) and the remote Pacific region (170º-180ºE, 19º-30ºS). The HCHO profiles over the remote Pacific region represent the background HCHO mixing ratio. CHASER and ATom background HCHO mixing ratio within the boundary layer are, respectively, 0.4 and 0.2 ppbv. The mean relative differences between the two datasets within the boundary layer over Amazonia and the remote Pacific region are ~60 and ~40%, indicating that the uncertainty in the contributions from the background and isoprene emissions to the total HCHO uncertainties is equivalent. Above 5 km, CHASER underestimates the background HCHO mixing ratios. However, simulated and TROPOMI HCHO columns over the remote Pacific regions showed consistency when gridded over a similar horizontal grid (Fig. 1). Consequently, differences in the horizontal resolution can cause the discrepancy between the simulations and ATom observations over the remote regions. Over

South America, the model overestimates the observed (TROPOMI and ATom) HCHO abundances irrespective of the horizontal resolution. Therefore, the biogenic emission estimates for South America in CHASER should be reviewed to reduce the model- observation biases.

3.8 Contribution estimates

The contributions of different VOC emission sources to the regional HCHO abundances are presented in Fig. 11. The contribution estimates are presented in Table 8. A stacked-bar plot of the annual contributions of the emission sources is portrayed in Fig. S9.

Over E-China, biomass burning has a non-significant effect on the regional HCHO columns. The biogenic and anthropogenic VOC emission contributions are, respectively, 44% and 17% during summer. In contrast, anthropogenic and biogenic contributions to the regional HCHO level during winter are, respectively 35% and 13%.

Non-significant biomass burning effects on the HCHO columns can be observed over E-USA, W-USA, and Europe. Biogenic emissions contribute more than 30% (40% in E-USA) in these regions. In Europe and W-USA, annual anthropogenic and biogenic contributions are equivalent. Although the simulated winter columns in these regions are consistent with TROPOMI (Fig. 2), the model values are lower during summer and autumn. Moreover, the sensitivity results show non-significant biogenic contribution during winter and autumn, which likely reduces the annual biogenic contribution estimates.

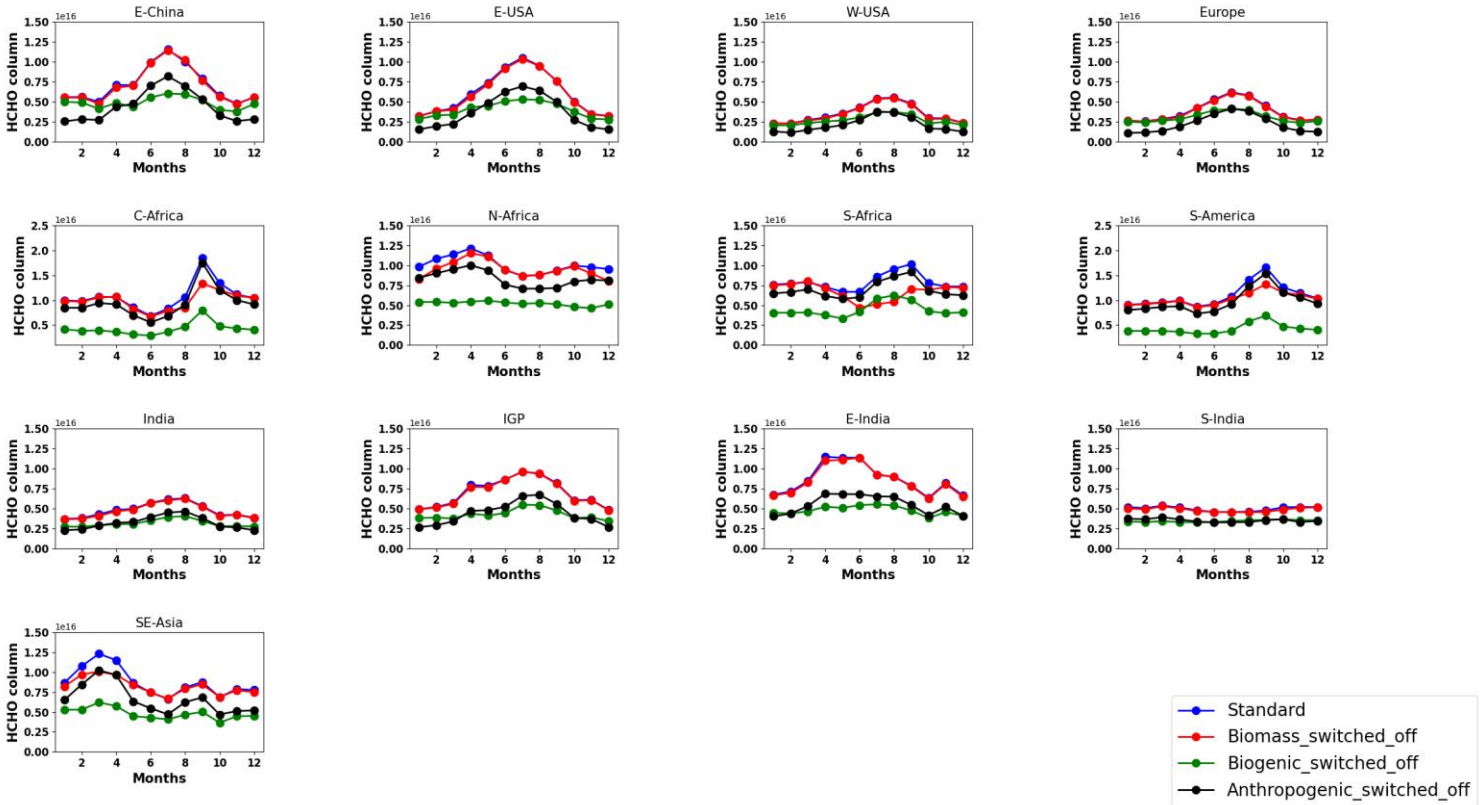

874

875 **Figure 11:** Seasonal variation of HCHO (× 10^{16} molecules cm^{-2}) inferred from different simulations. The settings
876 of the standard simulation are presented in Table 1. The model estimates shown in red, green, and blue are simulated
877 respectively by switching off the biomass-burning, biogenic, and anthropogenic emissions. The satellite AKs have
878 been applied to all the simulations. The coordinate bounds of the regions are similar to those in Fig. 2.

879 In C-Africa, biogenic emissions (60%) are the greatest contributor, followed by biomass burning
880 emissions (7%). Pyrogenic emissions contribute 26% (4.7 × 10^{15} molecules cm^{-2}) to the peak column in
881 September, whereas biogenic contributions are 55% (1 × 10^{16} molecules cm^{-2}). Although the biogenic
882 emission contributions are similar in N-Africa (43%) and S-Africa (47%), the pyrogenic contributions are
883 twice as high in the latter region. Consequently, despite similar HCHO abundances and modulation in
884 these regions, the source contributions differ.

885

886

887 **Table 8**. Contributions (%) of different emission sources to HCHO abundances in selected regions. The
888 respective emissions were switched off to estimate the contribution to the total HCHO abundances. The
889 contributions have been calculated with respect to the standard simulations. The satellite AKs were
890 applied to all simulations.
891

Region	**Biomass-burning contribution**	**Biogenic contribution**	**Anthropogenic contribution**
E-China	1.4%	31%	23%
E-USA	1.7%	34%	21%
W-USA	1.7%	23%	24%
Europe	1.5%	20%	22%
C-Africa	7%	60%	3%
N-Africa	6%	47%	9%
S-Africa	15%	43%	10%
S-America	7%	61%	5%
India	1.9%	34%	15%
IGP	1.1%	39%	13%

S-India	1.5%	44%	10%
E-India	1.6%	41%	11%
SE-Asia	6%	45%	7%

Over South America, biogenic emissions contribute 61% to the regional HCHO abundances. The pyrogenic contribution during the biomass burning period is 12%, whereas the annual contribution is 7%.

In SE-Asia, annual pyrogenic and anthropogenic contributions are equivalent (~6%). During the dry season, the anthropogenic, pyrogenic, and biogenic contributions are respectively 7%, 12%, and 48%. Biogenic production compromises 43% of the HCHO columns during July through December, whereas anthropogenic emissions account for 9%.

In India, annual pyrogenic emissions contribute ~2% to the HCHO levels. A similar source contribution to the HCHO levels in IGP is also observed. The model capability was limited in reproducing the observed HCHO seasonality in India and the IGP region. Consequently, robust source contribution estimates for these regions cannot be derived from the current analysis.

Over E-India, 41% of the HCHO levels originate from biogenic sources, followed by anthropogenic VOC emissions (11%). Similar source contributions of biogenic (44%) and anthropogenic (10%) emissions are observed in S-India. Over both regions, the pyrogenic source contribution is less than 2%.

4 Conclusions

CHASER simulated global HCHO spatiotemporal distributions at horizontal resolution of 2.8° × 2.8°were evaluated against multi-platform observations. First, two years of simulation results (2019–2020) were compared with the latest HCHO satellite observations from TROPOMI. The model–satellite agreement was excellent, with a global *r*-value of 0.93 and RMSE of 0.75×10^{15} molecules cm^{-2}. The model showed good capabilities for reproducing the HCHO columns in hotspot and background regions. CHASER HCHO columns over large forested areas showed good consistency with the observations, demonstrating that the biogenic emission estimates in the model are reasonable. Simulated HCHO seasonality in a few selected regions was consistent with the observations. The model was able to reproduce the observed wintertime HCHO columns in E-USA, W-USA, and Europe, in addition to summer peaks. Disagreement between TROPOMI and CHASER was observed primarily in India, China, Amazonia, and SE Asia. Uncertainties in background HCHO columns, anthropogenic VOC emission inventories, chemical mechanisms adopted in the model, and retrieval algorithms were the potential contributors to these discrepancies. However, such uncertainties did not affect the model–satellite agreement in Africa and South America. Comparison among OMI, TROPOMI, and CHASER HCHO columns demonstrated that TROPOMI's improved spatial resolution effect was limited globally. However, in most regions, simulated HCHO seasonality showed better agreement with TROPOMI than with OMI, reducing the RMSE by up to 63%. TROPOMI retrievals were, on average, 30% lower than those of OMI.

Second, CHASER simulations were compared with two-year MAX-DOAS observations of HCHO at Phimai, Chiba, and Kasuga. Daily CHASER HCHO mixing ratios showed consistency with the observations at the three sites, with *R*-values of 0.39–0.67. The slopes of linear fitting were lower for Chiba (0.29) and Kasuga (0.29) than for Phimai (0.37), implying lower model underestimation at the latter site. The diurnal variations at the sites were consistent with the observations. The change in the NO_x emission inventories did not affect the simulated diurnal variations.

Third, simulated HCHO and isoprene profiles for 2018 were compared with ATom-4 flight observations. Despite consistent profile shapes, the model overestimated VOC mixing ratios mainly within the PBL. Uncertainties related to VOC emission inventories, background HCHO levels, and model resolution were potential reasons for the model–flight discrepancies.

Lastly, sensitivity studies were conducted to estimate the contributions of the different emissions sources to the total HCHO columns in different regions. Biogenic emissions were the greatest contributor in most of the regions. In a few cases, biogenic and anthropogenic emission contributions were equivalent. In some regions, except during the summer, the model was less sensitive to changes in the biogenic emissions, likely reducing the biogenic contributions.

Code availability. The CHASER and JM2 source codes are not available publicly. Dr. Kengo Sudo (kengo@nagoya-u.jp) is the contact person for readers and researchers interested in the CHASER model. In addition, Dr. Hitoshi Irie (hitoshi.irie@chiba-u.jp) will answer queries regarding using the JM2 codes.

Data availability: The model simulations and observational datasets used for the evaluation study are available on the Zenodo website (Hoque et al., 2024). The MAX-DOAS profile and column data can be obtained through personal communication from Dr. Hitoshi Irie (hitoshi.irie@chiba-u.jp). TROPOMI (https://scihub.copernicus.eu/dhus/#/home, last access: 01 July 2023; De Smedt et al., 2021), OMI BIRA product, (https://www.temis.nl/qa4ecv/hcho/hcho_omi.php, last access: 01 July 2023; De Smedt et al., 2021) and ATom(https://daac.ornl.gov/ATOM/guides/ATom_nav.html, last access: 01 July 2023; Wofsy et al., 2018) data are publicly available.

Author contributions*:* HMSH conceptualized the study, conducted the model simulations, analyzed the datasets, and drafted the manuscript. YH helped with the data processing. HI developed the JM2 code and maintained the A-SKY network. KS developed the CHASER model and supervised the study. MFK extended his expertise to explain the results. All the authors commented and provided feedback on the final results and manuscript.

Conflict of Interest: The authors declare that they have no conflict of interest

Acknowledgments: We are grateful to the TROPOMI, OMI, and ATom scientific teams for making the respective observational datasets available for public usage. The CHASER model simulations are partly performed with the supercomputer (NEC SX-Aurora TSUBASA) at the National Institute for Environmental Studies (NIES), Tsukuba, Japan. The corresponding author acknowledges the valuable advice of Dr. Kazuyakai Miyazaki (Jet Propulsion Lab, NASA) and Dr. Takashi Sekiya (JAMSTEC, Japan). The research has been supported by the Ministry of the Environment, Government of Japan

(Global Environmental Research Fund (grant nos. S-12 and S-20)), the Japan Society for the Promotion of Science (KAKENHI (grant nos. JP20H04320, JP19H05669, JP19HO4235, JP23H04971, JP21K12227, JP22H03727, and JP22H05004)), the Environment Research and Technology Development Fund (JPMEERF20215005) of the Environmental Restoration and Conservation Agency of Japan, and the JAXA 3rd research announcement on the Earth observations (grant number 19RT000351).

References

Apel, E. C., Asher, E. C., Hills, A. J., and Hornbrook, R. S. : ATom: Volatile Organic Compounds (VOCs) from the TOGA instrument, Version 2, ORNL DAAC, Oak Ridge, Tennessee, USA, https://doi.org/10.3334/ORNLDAAC/1936, 2021

Arlander, D., Brüning, D., Schmidt, U., & Ehhalt, D. :The tropospheric distribution of formaldehyde during TROPOZ II. J. Atmos. Chem., 22(3), 251-269. https://doi.org/10.1007/BF00696637, 1995

Bauwens, M., Verreyken, B., Stavrakou, T., Müller, J., & De Smedt, I.: Spaceborne evidence for significant anthropogenic VOC trends in Asian cities over 2005–2019. Environ. Res. Lett., 17(1), 015008. doi:https://iopscience.iop.org/article/10.1088/1748-9326/ac46eb/, 2022

Boersma, K. F., Eskes, H. J., and Brinksma, E. J. : Error analysis for tropospheric NO_2 retrieval from space. J. Geophys. Res., 109, D04311. https://doi.org/10.1029/2003JD003962, 2004

Burkert, J., Andrés-Hernández,M.D., Stöbener,D., Burrows,J.P., Weissenmayer,M., & Kraus,A. : Peroxy radical and related trace gas measurements in the boundary layer above the Atlantic Ocean.J. Geophys. Res., 106(D6): 5457-5477. https://doi.org/10.1029/2000JD900613, 2001

Burrows, J. P., Weber, M., Buchwitz, M., Rozanov, V., Ladstätter-Weißenmayer, A., Richter, A., DeBeek, R., Hoogen, R., Bramstedt, K., Eichmann, K-U Eisinger, M., & Perner, D. : The Global Ozone Monitoring Experiment (GOME): Mission Concept and First Scientific Results. J. Atmos. Sci. 56(2), 151-175. doi:https://doi.org/10.1175/1520-0469(1999)056<0151:TGOMEG>2.0.CO;2, 1999

Caballero, C. B., Ruhoff, A. and Biggs, T.: Land use and land cover changes and their impacts on surface-atmosphere interactions in Brazil: A systematic review, Sci. Total Environ. 808: 152134, https://doi.org/10.1016/j.scitotenv.2021.152134, 2022

Cazorla, M., Wolfe, G. M., Bailey, S. A., Swanson, A. K., Arkinson, H. L., and Hanisco, T. F.: A new airborne laser-induced fluorescence instrument for in situ detection of formaldehyde throughout the troposphere and lower stratosphere, Atmos. Meas. Tech.., 8, 541–552, https://doi.org/10.5194/amt-8-541-2015, 2015.

Chan, K. L., Wiegner, M., van Geffen, J., De Smedt, I., Alberti, C., Cheng, Z., Ye, S., & Wenig, M. : MAX-DOAS measurements of tropospheric NO2 and HCHO in Munich and the comparison to OMI and TROPOMI satellite observations. Atmos. Meas. Tech., 13(8), 4499-4520. doi:10.5194/amt-13-4499-2020, 2020

Colella, P., & Woodward, P. R. : The piecewise parabolic method (PPM) for gas-dynamical simulations. J. Comput. Phys.., 54(1), 174-201. doi:https://doi.org/10.1016/0021-9991(84)90143-8, 1984

Crippa, M., Guizzardi, D., Butler, T., Keating, T., Wu, R., Kaminski, J., Kuenen, J., Kurokawa, J., Chatani, S., Morikawa, T., Pouliot, G., Racine, J., Moran, M. D., Klimont, Z., Manseau, P. M., Mashayekhi, R., Henderson, B. H., Smith, S. J., Suchyta, H., Muntean, M., Solazzo, E., Banja, M., Schaaf, E., Pagani, F., Woo, J.-H., Kim, J., Monforti-Ferrario, F., Pisoni, E., Zhang, J., Niemi, D., Sassi, M.,

Ansari, T., and Foley, K.: The HTAP_v3 emission mosaic: merging regional and global monthly emissions (2000–2018) to support air quality modelling and policies, Earth Syst. Sci. Data, 15, 2667–2694, https://doi.org/10.5194/essd-15-2667-2023, 2023

De Smedt, I., Pinardi, G., Vigouroux, C., Compernolle, S., Bais, A., Benavent, N., Boersma, F., Chan, K.-L., Donner, S., Eichmann, K.-U., Hedelt, P., Hendrick, F., Irie, H., Kumar, V., Lambert, J.-C., Langerock, B., Lerot, C., Liu, C., Loyola, D., Piters, A., Richter, A., Rivera Cárdenas, C., Romahn, F., Ryan, R. G., Sinha, V., Theys, N., Vlietinck, J., Wagner, T., Wang, T., Yu, H., and Van Roozendael, M. : Comparative assessment of TROPOMI and OMI formaldehyde observations and validation against MAX-DOAS network column measurements, Atmos. Chem. Phys., 21, 12561–12593, https://doi.org/10.5194/acp-21-12561-2021, 2021

De Smedt, I., Theys, N., Yu, H., Danckaert, T., Lerot, C., Compernolle, S., Van Roozendael, M., Richter, A., Hilboll, A., Peters, E., Pedergnana, M., Loyola, D., Beirle, S., Wagner, T., Eskes, H., van Geffen, J., Boersma, K. F., & Veefkind, P. : Algorithm theoretical baseline for formaldehyde retrievals from S5P TROPOMI and from the QA4ECV project. Atmos. Meas. Tech., 11, 2395–2426. https://doi.org/10.5194/amt-11-2395-2018, 2018, 2018

De Smedt, I., Yu, H., Richter, A., Beirle, S., Eskes, H., Boersma, K.F., Van Roozendael, M., Van Geffen, J., Lorente, A., & Peters, E. : QA4ECV HCHO tropospheric column data from OMI (Version 1.1) [Data set], Royal Belgian Institute for Space Aeronomy. https://doi.org/10.18758/71021031, 2017

De Smedt, I., Stavrakou, T., Müller, J.-F., van der A, R. J., & Van Roozendael, M. : Trend detection in satellite observations of formaldehyde tropospheric columns. Geophys. Res. Lett., 37(18). doi:https://doi.org/10.1029/2010GL044245, 2010

De Smedt, I., Müller, J. F., Stavrakou, T., van der A, R., Eskes, H., & Van Roozendael, M. : Twelve years of global observations of formaldehyde in the troposphere using GOME and SCIAMACHY sensors. Atmos. Chem. Phys., 8(16), 4947-4963. doi:10.5194/acp-8-4947-2008, 2008

Emori, S., Nozawa, T., Numaguti, A., & Uno, I. : Importance of cumulus parameterization for precipitation simulation over East Asia in June, 79(4), 939-947. doi:https://doi.org/10.2151/jmsj.79.939, 2021

Franco, B., Hendrick, F., Van Roozendael, M., Müller, J.-F., Stavrakou, T., Marais, E. A., Bovy, B., Bader, W.,Fayt, C., Hermans, C. ,Lejuene, B. ,Pinardi, G. ,Sevais, C. , & Mahieu, E. : Retrievals of formaldehyde from ground-based FTIR and MAX-DOAS observations at the Jungfraujoch station and comparisons with GEOS-Chem and IMAGES model simulations. Atmos. Meas. Tech., 8(4), 1733-1756. doi:https://doi.org/10.5194/amt-8-1733-2015, 2015

Fu, T. M., Jacob, D. J., Wittrock, F., Burrows, J. P., Vrekoussis, M., & Henze, D. K. : Global budgets of atmospheric glyoxal and methylglyoxal, and implications for formation of secondary organic aerosols.J. Geophys. Res., 113(D15). doi: https://doi.org/10.1029/2007JD009505, 2008

González Abad, G., Vasilkov, A., Seftor, C., Liu, X., & Chance, K. : Smithsonian Astrophysical Observatory Ozone Mapping and Profiler Suite (SAO OMPS) formaldehyde retrieval. Atmos. Meas. Tech., 9(7), 2797-2812. doi:10.5194/amt-9-2797-2016, 2016

Guenther, A., Karl, T., Harley, P., Wiedinmyer, C., Palmer, P. I., and Geron, C. :Estimates of global terrestrial isoprene emissions using MEGAN (Model of Emissions of Gases and Aerosols from Nature), Atmos. Chem. Phys. 6, 3181–3210, https://doi.org/10.5194/acp-6-3181-2006, 2006

Ha, P. T. M., Kanaya, Y., Taketani, F., Andrés Hernández, M. D., Schreiner, B., Pfeilsticker, K., and Sudo, K.: Implementation of HONO into the chemistry–climate model CHASER (V4.0): roles in tropospheric chemistry: Geosci. Model Dev. 16, 927–960, https://doi.org/10.5194/gmd-16-927-2023, 2023

Hak, C., Pundt, I., Trick, S., Kern, C., Platt, U., Dommen, J., Ordóñez, C., Prévôt, A. S. H., Junkermann, W., Astorga-Lloréns, C., Larsen, B. R., Mellqvist, J., Strandberg, A., Yu, Y., Galle, B., Kleffmann, J., Lörzer, J. C., Braathen, G. O., & Volkamer, R. : Intercomparison of four different in-situ techniques for ambient formaldehyde measurements in urban air. Atmos. Chem. Phys., 5(11), 2881-2900. doi:https://doi.org/10.5194/acp-5-2881-2005, 2005

Ito, A., & Inatomi, M.: Use of a process-based model for assessing the methane budgets of global terrestrial ecosystems and evaluation of uncertainty. Biogeosciences, 9(2), 759-773. doi:https://doi.org/10.5194/bg-9-759-2012, 2012

He, Y., Hoque, H. M. S., and Sudo, K.: Introducing new lightning schemes into the CHASER (MIROC) chemistry–climate model (2022). Geosci. Model Dev.t, 15, 5627–5650, https://doi.org/10.5194/gmd-15-5627-2022, 2022

Hoque, H. M. S., Sudo, K., and Irie, H., : Model and observational datasets used for evaluating CHASER simulated formaldehyde (HCHO) abundances in 2019 and 2020. [Dataset]. Zenodo. https://doi.org/10.5281/zenodo.10052384, 2024

Hoque, H. M. S., Sudo, K., Irie, H., Damiani, A., Naja, M., and Fatmi, A. M. : Multi-axis differential optical absorption spectroscopy (MAX-DOAS) observations of formaldehyde and nitrogen dioxide at three sites in Asia and comparison with the global chemistry transport model CHASER, Atmos. Chem. Phys., 22, 12559–12589, https://doi.org/10.5194/acp-22-12559-2022, 2022

Hoque, H., Irie, H., & Damiani, A. : First MAX-DOAS Observations of Formaldehyde and Glyoxal in Phimai, Thailand. J. Geophys. Res., 123(17), 9957-9975. doi: https://doi.org/10.1029/2018JD028480,a, 2018a

Hoque, H. M. S., Irie, H., Damiani, A., Rawat, P., & Naja, M.: First simultaneous observations of formaldehyde and glyoxal by MAX-DOAS in the Indo-Gangetic Plain region. Sola. doi:https://doi.org/10.2151/sola.2018-028,b, 2018b

Irie, H. (2021). International air quality and sky research remote sensing network (A-SKY): Its development and satellite atmosphere product validation, Journal of the Remote Sensing Society of Japan, 41, 5, 575-581, https://doi.org/10.11440/rssj.41.575, 2021a

Irie, H., D. Yonekawa, A. Damiani, H. M. S. Hoque, K. Sudo and S. Itahashi : Continuous multi-component MAX-DOAS observations for the planetary boundary layer ozone variation analysis at Chiba and Tsukuba, Japan, from 2013 to 2019. Prog. Earth Planet. Sci., 8(1): 1-11., 2021b

Irie, H., Nakayama, T., Shimizu, A., Yamazaki, A., Nagai, T., Uchiyama, A., Zaizen, Y., Kagamitani, S., & Matsumi, Y. : Evaluation of MAX-DOAS aerosol retrievals by coincident observations using CRDS, lidar, and sky radiometer in Tsukuba, Japan. Atmos. Meas. Tech., 8(7), 2775-2788. doi:https://doi.org/10.5194/amt-8-2775-2015, 2015

Irie, H., Takashima, H., Kanaya, Y., Boersma, K., Gast, L., Wittrock, F., Brunner, D., Zhou, Y., & Roozendael, M. V. : Eight-component retrievals from ground-based MAX-DOAS observations. Atmos. Meas. Tech.., 4(6), 1027-1044. doi:https://doi.org/10.5194/amt-4-1027-2011, 2011

Irie, H., Kanaya, Y., Akimoto, H., Iwabuchi, H., Shimizu, A., & Aoki, K. : First retrieval of tropospheric aerosol profiles using MAX-DOAS and comparison with lidar and sky radiometer measurements. Atmos. Chem. Phys., 8(2), 341-350. doi:https://doi.org/10.5194/acp-8-341-2008, 2008

Jenkin, M. E., Young, J. C., & Rickard, A. R. The MCM v3. 3.1 degradation scheme for isoprene. Atmos. Chem. Phys., 15(20), 11433-11459. doi:https://doi.org/10.5194/acp-15-11433-201, 2015

Khan, M. F., Latif, M., Saw, W., Amil, N., Nadzir, M., Sahani, M., Tahir, N.M., & Chung, J. : Fine particulate matter associated with monsoonal effect and the responses of biomass fire hotspots in the tropical environment. Atmos. Chem. Phys., 16, 597–617, https://doi.org/10.5194/acp-16-597-2016, 2016

Kleipool, Q. L., Dobber, M. R., de Haan, J. F., and Levelt, P. F.: Earth surface reflectance climatology from 3 years of OMI data, J. Geophys. Res., 113, D18308. https://doi.org/10.1029/2008JD010290, 2008

Kreher, K., Van Roozendael, M., Hendrick, F., Apituley, A., Dimitropoulou, E., Frieß, U., Richter, A., Wagner, T., Lampel, J., Abuhassan, N., Ang, L., Anguas, M., Bais, A., Benavent, N., Bösch, T., Bognar, K., Borovski, A., Bruchkouski, I., Cede, A., Chan, K. L., Donner, S., Drosoglou, T., Fayt, C., Finkenzeller, H., Garcia-Nieto, D., Gielen, C., Gómez-Martín, L., Hao, N., Henzing, B., Herman, J. R., Hermans, C., Hoque, S., Irie, H., Jin, J., Johnston, P., Khayyam Butt, J., Khokhar, F., Koenig, T. K., Kuhn, J., Kumar, V., Liu, C., Ma, J., Merlaud, A., Mishra, A. K., Müller, M., Navarro-Comas, M., Ostendorf, M., Pazmino, A., Peters, E., Pinardi, G., Pinharanda, M., Piters, A., Platt, U., Postylyakov, O., Prados-Roman, C., Puentedura, O., Querel, R., Saiz-Lopez, A., Schönhardt, A., Schreier, S. F., Seyler, A., Sinha, V., Spinei, E., Strong, K., Tack, F., Tian, X., Tiefengraber, M., Tirpitz, J.-L., van Gent, J., Volkamer, R., Vrekoussis, M., Wang, S., Wang, Z., Wenig, M., Wittrock, F., Xie, P. H., Xu, J., Yela, M., Zhang, C., and Zhao, X. : Intercomparison of NO_2, O_4, O_3 and HCHO slant column measurements by MAX-DOAS and zenith-sky UV–visible spectrometers during CINDI-2. Atmos. Meas. Tech., 13, 2169–2208, https://doi.org/10.5194/amt-13-2169-2020, 2020

Kumar, A., Hakkim, H., Ghude, S. D., & Sinha, V. : Probing wintertime air pollution sources in the Indo-Gangetic Plain through 52 hydrocarbons measured rarely at Delhi & Mohali. Sci. Total Environ., 801, 149711. doi:https://doi.org/10.1016/j.scitotenv.2021.149711, 2021

Kupc, A., Williamson, C., Wagner, N. L., Richardson, M., and Brock, C. A.: Modification, calibration, and performance of the Ultra-High Sensitivity Aerosol Spectrometer for particle size distribution and volatility measurements during the Atmospheric Tomography Mission (ATom) airborne campaign. Atmos. Meas. Tech., 11, 369–383, https://doi.org/10.5194/amt-11-369-2018, 2018

Kurucz, R. L., Furenlid, I., Brault, J., and Testerman, L., Solar flux atlas from 296 to 1300 nm. National Solar Observatory Atlas No. 1, Sunspot, New Mexico, 1984

Kuttippurath, J., Abbhishek, K., Gopikrishnan, G. S., & Pathak, M. : Investigation of long–term trends and major sources of atmospheric HCHO over India. Environ. Chall., 7, 100477. doi:https://doi.org/10.1016/j.envc.2022.100477, 2022

Lee, M., Heikes, B. G., Jacob, D. J., Sachse, G., & Anderson, B.: Hydrogen peroxide, organic hydroperoxide, and formaldehyde as primary pollutants from biomass burning, J. Geophys. Res., 102(D1), 1301-1309. doi: https://doi.org/10.1029/96JD01709, 1997

Levelt, P. F., Joiner, J., Tamminen, J., Veefkind, J. P., Bhartia, P. K., Stein Zweers, D. C., Duncan, B. N., Streets, D. G., Eskes, H., van der A, R., McLinden, C., Fioletov, V., Carn, S., de Laat, J., DeLand, M., Marchenko, S., McPeters, R., Ziemke, J., Fu, D., Liu, X., Pickering, K., Apituley, A., González Abad, G., Arola, A., Boersma, F., Chan Miller, C., Chance, K., de Graaf, M., Hakkarainen, J., Hassinen, S., Ialongo, I., Kleipool, Q., Krotkov, N., Li, C., Lamsal, L., Newman, P., Nowlan, C., Suleiman, R., Tilstra, L. G., Torres, O., Wang, H., & Wargan, K., : The Ozone Monitoring Instrument: overview of 14 years in space, Atmos. Chem. Phys., 18, 5699–5745, https://doi.org/10.5194/acp-18-5699-2018, 2018

Levelt, P. F., Stein Zweers, D. C., Aben, I., Bauwens, M., Borsdorff, T., De Smedt, I., Eskes, H. J., Lerot, C., Loyola, D. G., Romahn, F., Stavrakou, T., Theys, N., Van Roozendael, M., Veefkind, J. P., and Verhoelst, T.: Air quality impacts of COVID-19 lockdown measures detected from space using high spatial resolution observations of multiple trace gases from Sentinel-5P/TROPOMI, Atmos. Chem. Phys., 22, 10319–10351, https://doi.org/10.5194/acp-22-10319-2022, 2022

Liu, F., Q. Zhang, R. J. van der A, B. Zheng, D. Tong, L. Yan, Y. Zheng and K. He : Recent reduction in NOx emissions over China: synthesis of satellite observations and emission inventories. Environ. Res. Lett.,11(11): 114002. doi: 10.1088/1748-9326/11/11/114002, 2016

Liu, Y., Wang, H., Jing, S., Peng, Y., Gao, Y., Yan, R., Wang, Q., Lou, S., Cheng, T., & Huang, C.: Strong regional transport of volatile organic compounds (VOCs) during wintertime in Shanghai megacity of China. Atmos. Environ., 244, 117940. doi:https://doi.org/10.1016/j.atmosenv.2020.117940, 2021

Luecken, D. J., Napelenok, S. L., Strum, M., Scheffe, R., & Phillips, S.: Sensitivity of Ambient Atmospheric Formaldehyde and Ozone to Precursor Species and Source Types Across the United States. Environ. Sci. Tech., 52(8), 4668-4675. doi:10.1021/acs.est.7b05509, 2018

Meller, R. & Moortgat, G. K. : Temperature dependence of the absorption cross section of HCHO between 223 and 323 K in the wavelength range 225–375 nm, J. Geophys. Res., 105, 7089–7102. https://doi.org/10.1029/1999JD901074, 2000

Mellor, G. L., & Yamada, T. : A hierarchy of turbulence closure models for planetary boundary layers. J. Atmos. Sci., 31(7), 1791-1806. doi:https://doi.org/10.1175/1520-0469(1974)031<1791:AHOTCM>2.0.CO;2. 1974

Miyazaki, K., Eskes, H., Sudo, K., Boersma, K. F., Bowman, K., & Kanaya, Y. : Decadal changes in global surface NOx emissions from multi-constituent satellite data assimilation. Atmos. Chem. Phys., 17(2), 807-837. doi:https://doi.org/10.5194/acp-17-807-2017, 2017

Miyazaki, K., Bowman, K., Sekiya, T., Eskes, H., Boersma, F., Worden, H., Livesey, N., Payne, V. H., Sudo, K., Kanaya, Y., & Takigawa, M. Ogochi, K. : Updated tropospheric chemistry reanalysis and emission estimates, TCR-2, for 2005–2018. Earth Syst. Sci. Data, 12(3), 2223-2259. doi:10.5194/essd-12-2223-2020, 2020

Müller, J.-F., Stavrakou, T., Wallens, S., De Smedt, I., Van Roozendael, M., Potosnak, M. J., Rinne, J., Munger, B., Goldstein, A., & Guenther, A. B. : Global isoprene emissions estimated using MEGAN, ECMWF analyses and a detailed canopy environment model, Atmos. Chem. Phys., 8, 1329–1341, https://doi.org/10.5194/acp-8-1329-2008, 2008

Munro, R., Lang, R., Klaes, D., Poli, G., Retscher, C., Lindstrot, R., Huckle, R. ,Lacan, A., Grzegorski, M., Holdak, A., Kokhanovsky, A., Livschitz, J., & Eisinger, M.: The GOME-2 instrument on the Metop series of satellites: instrument design, calibration, and level 1 data processing – an overview. Atmos. Meas. Tech., 9(3), 1279-1301. doi:10.5194/amt-9-1279-2016, 2016

Opacka, B., Müller, J. F., Stavrakou, T., Bauwens, M., Sindelarova, K., Markova, J., & Guenther, A. B.: Global and regional impacts of land cover changes on isoprene emissions derived from spaceborne data and the MEGAN model. Atmos. Chem. Phys., 21(11), 8413-8436. doi:10.5194/acp-21-8413-2021, 2021

Price, C., & Rind, D. : A simple lightning parameterization for calculating global lightning distributions.J. Geophys. Res., 97(D9), 9919-9933. doi: https://doi.org/10.1029/92JD00719, 1992

Possanzini, M., Palo, V. D., & Cecinato, A. (2002). Sources and photodecomposition of formaldehyde and acetaldehyde in Rome ambient air. Atmos. Environ., 36(19), 3195-3201. doi:https://doi.org/10.1016/S1352-2310(02)00192-9

Roberts, G., Wooster, M. J., and Lagoudakis, E.: Annual and diurnal African biomass burning temporal dynamics, Biogeosciences, 6, 849–866. https://doi.org/10.5194/bg-6-849-2009, 2009

Roscoe, H. K., Van Roozendael, M., Fayt, C., du Piesanie, A., Abuhassan, N., Adams, C., Akrami, M., Cede, A., Chong, J., Clémer, K., Friess, U., Gil Ojeda, M., Goutail, F., Graves, R., Griesfeller, A.,

Grossmann, K., Hemerijckx, G., Hendrick, F., Herman, J., Hermans, C., Irie, H., Johnston, P. V., Kanaya, Y., Kreher, K., Leigh, R., Merlaud, A., Mount, G. H., Navarro, M., Oetjen, H., Pazmino, A., Perez-Camacho, M., Peters, E., Pinardi, G., Puentedura, O., Richter, A., Schönhardt, A., Shaiganfar, R., Spinei, E., Strong, K., Takashima, H., Vlemmix, T., Vrekoussis, M., Wagner, T., Wittrock, F., Yela, M., Yilmaz, S., Boersma, F., Hains, J., Kroon, M., Piters, A., and Kim, Y. J. : Intercomparison of slant column measurements of NO_2 and O_4 by MAX-DOAS and zenith-sky UV and visible spectrometers, Atmos. Meas. Tech., 3, 1629–1646, https://doi.org/10.5194/amt-3-1629-2010, 2010

Ryan, R. G., Silver, J. D., Querel, R., Smale, D., Rhodes, S., Tully, M., Jones, N., & Schofield, R.: Comparison of formaldehyde tropospheric columns in Australia and New Zealand using MAX-DOAS, FTIR and TROPOMI. Atmos. Meas. Tech., 13(12), 6501-6519. doi:10.5194/amt-13-6501-2020, 2020

Salazar, D., Lokvam, J., Mesones, I., Vásquez Pilco, M., Ayarza Zuñiga, J. M., de Valpine, P., & Fine, P. V. A. : Origin and maintenance of chemical diversity in a species-rich tropical tree lineage. Nat. Ecol. Evol., 2(6), 983–990. https://doi.org/10.1038/s4155 9-018-0552-0, 2018

Sekiya, T., Miyazaki, K., Eskes, H., Bowman, K., Sudo, K., Kanaya, Y., & Takigawa, M. : The worldwide COVID-19 lockdown impacts on global secondary inorganic aerosols and radiative budget. Sci. Adv., 9(30), eadh2688. doi:doi:10.1126/sciadv.adh2688, 2023

Sekiya, T., Miyazaki, K., Ogochi, K., Sudo, K., & Takigawa, M. : Global high-resolution simulations of tropospheric nitrogen dioxide using CHASER V4.0. Geosci. Model Dev., 11(3), 959-988. doi:10.5194/gmd-11-959-2018, 2018

Sekiya, T., & Sudo, K. : Roles of transport and chemistry processes in global ozone change on interannual and multidecadal time scales.J. Geophys. Res., 119(8), 4903-4921. doi:https://doi.org/10.1002/2013JD020838, 2014

Simpson, I. J., Blake, D. R., Blake, N. J., Meinardi, S., Barletta, B., Hughes, S. C., Fleming, L. T., Crawford, J. H., Diskin, G. S., Emmons, L. K., Fried, A., Guo, H., Peterson, D. A., Wisthaler, A., Woo, J.-H., Barré, J., Gaubert, B., Kim, J., Kim, M. J., Kim, Y., Knote, C., Mikoviny, T., Pusede, S. E., Schroeder, J. R., Wang, Y., Wennberg, P. O., and Zeng, L.: Characterization, sources, and reactivity of volatile organic compounds (VOCs) in Seoul and surrounding regions during KORUS-AQ, Elementa, 8, 37, https://doi.org/10.1525/elementa.434,, 2020

Sindelarova, K., Markova, J., Simpson, D., Huszar, P., Karlicky, J., Darras, S., & Granier, C.: High-resolution biogenic global emission inventory for the time period 2000–2019 for air quality modeling., 14(1), 251-270. doi:https://doi.org/10.5194/essd-14-251-2022, 2022

Singh, H., Salas, L., Chatfield, R., Czech, E., Fried, A., Walega, J., Evans, M., Field, B., Jacob, D., & Blake, D.: Analysis of the atmospheric distribution, sources, and sinks of oxygenated volatile organic chemicals based on measurements over the Pacific during TRACE-P.J. Geophys. Res.. 109(D15). doi:https://doi.org/10.1029/2003JD003883, 2004

Sinreich, R., Frieß, U., Wagner, T., & Platt, U.: Multi-axis differential optical absorption spectroscopy (MAX-DOAS) of gas and aerosol distributions. Faraday discussions., 130, 153-164. doi:https://doi.org/10.1039/B419274P, 2005

Souri, A. H., Chance, K., Bak, J., Nowlan, C. R., González Abad, G., Jung, Y., Wong, D. C., Mao, J., & Liu, X.: Unraveling pathways of elevated ozone induced by the 2020 lockdown in Europe by an observationally constrained regional model using TROPOMI, Atmos. Chem. Phys., 21, 18227–18245, https://doi.org/10.5194/acp-21-18227-2021, 2021

Spurr, R. J. D. : LIDORT and VLIDORT: Linearized pseudo-spherical scalar and vector discrete ordinate radiative transfer models for use in remote sensing retrieval problems. Light Scattering Reviews, edited by: Kokhanovsky, A., 229–271, Berlin, Springer, 2008

Stavrakou, T., Müller, J.-F., Bauwens, M., De Smedt, I., Van Roozendael, M., De Mazière, M., Vigouroux, C., Hendrick, F., George, M., Clerbaux, C., Coheur, P.-F., and Guenther, A.:How consistent are top-down hydrocarbon emissions based on formaldehyde observations from GOME-2 and OMI? Atmos. Chem. Phys., 15, 11861–11884, https://doi.org/10.5194/acp-15-11861-2015, 2015

Sudo, K., Takahashi, M., Kurokawa, J., & Akimoto, H. : CHASER: A global chemical model of the troposphere 1. Model description.J. Geophys. Res., 107(D17), ACH 7-1-ACH 7-20. doi: https://doi.org/10.1029/2001JD001113, 2002

Sudo, K., & Akimoto, H.: Global source attribution of tropospheric ozone: Long-range transport from various source regions.J. Geophys. Res., 112(D12). doi:https://doi.org/10.1029/2006JD007992, 2007

Sun, W., Zhu, L., De Smedt, I., Bai, B., Pu, D., Chen, Y., et al. : Global significant changes in formaldehyde (HCHO) columns observed from space at the early stage of the COVID-19 pandemic. Geophys. Res. Lett., 48, e2020GL091265. https://doi.org/10.1029/2020GL091265 , 2021

Surl, L., Palmer, P. I., & González Abad, G.: Which processes drive observed variations of HCHO columns over India? Atmos. Chem. Phys., 18(7), 4549-4566. doi:https://doi.org/10.5194/acp-18-4549-2018, 2018

Takemura, T., Nozawa, T., Emori, S., Nakajima, T. Y., & Nakajima, T. : Simulation of climate response to aerosol direct and indirect effects with aerosol transport-radiation model. J. Geophys. Res., 110(D2). doi:https://doi.org/10.1029/2004JD005029, 2005

Takemura, T., Egashira, M., Matsuzawa, K., Ichijo, H., O'ishi, R., & Abe-Ouchi, A. : A simulation of the global distribution and radiative forcing of soil dust aerosols at the Last Glacial Maximum, Atmos. Chem. Phys., 9(9), 3061-3073. doi:https://doi.org/10.5194/acp-9-3061-2009, 2009

Taylor, T. C., McMahon, S. M., Smith, M. N., Boyle, B., Violle, C., van Haren, J., Simova, I., Meir,P., Ferreira, L.V., de Camargo, P.B., da Costa, A.C.L., Enquist, B.J., and Saleska, S. R. : Isoprene emission structures tropical tree biogeography and community assembly responses to climate. New Phytol., 220(2), 435–446, https://doi.org/10.1111/ nph.15304, 2018

Thornton, B. F., Wik, M., and Crill, P. M. : Double-counting challenges the accuracy of high-latitude methane inventories, Geophys. Res. Lett.., 43, 12,569– 12,577, doi:10.1002/2016GL071772, 2016

Weller, R., Schrems, O., Boddenberg, A., Gäb, S. & Gautrois, M. : Meridional distribution of hydroperoxides and formaldehyde in the marine boundary layer of the Atlantic (48° N-35° S) measured during the Albatross campaign. J. Geophys. Res., 105(D11): 14401-14412. https://doi.org/10.1029/1999JD901145, 2000

Veefkind, J. P., Aben, I., McMullan, K., Förster, H., de Vries, J., Otter, G., Claas, J. ,Eskes, H. J., de Haan, J. F.,Kleipool, Q., van Weele, M., Hasekamp, O., Hoogeveen, R., Landgraf, J., Snel, R., Tol, P., Ingmann, P., Voors, R., Kruizinga, B., Vink, R., Visser, H., & Levelt, P. F.: TROPOMI on the ESA Sentinel-5 Precursor: A GMES mission for global observations of the atmospheric composition for climate, air quality, and ozone layer applications. Remote Sens. Environ. 120, 70-83. doi:https://doi.org/10.1016/j.rse.2011.09.027, 2012

Vigouroux, C., Langerock, B., Bauer Aquino, C. A., Blumenstock, T., Cheng, Z., De Mazière, M., De Smedt, I., Grutter, M., Hannigan, J. W., Jones, N., Kivi, R., Loyola, D., Lutsch, E., Mahieu, E., Makarova, M., Metzger, J.-M., Morino, I., Murata, I., Nagahama, T., Notholt, J., Ortega, I., Palm, M., Pinardi, G., Röhling, A., Smale, D., Stremme, W., Strong, K., Sussmann, R., Té, Y., van Roozendael, M., Wang, P., & Winkler, H., :TROPOMI–Sentinel-5 Precursor formaldehyde validation using an extensive network of ground-based Fourier-transform infrared stations, Atmos. Meas. Tech., 13, 3751–3767, https://doi.org/10.5194/amt-13-3751-2020, 2020

Vrekoussis, M., Wittrock, F., Richter, A., & Burrows, J. : GOME-2 observations of oxygenated VOCs: what can we learn from the ratio glyoxal to formaldehyde on a global scale? Atmos. Chem. Phys., 10(21), 10145-10160. doi:https://doi.org/10.5194/acp-10-10145-2010, 2010

Wesely, M. : Parameterization of surface resistances to gaseous dry deposition in regional-scale numerical models. Atmos. Environ., 41, 52-63. doi:https://doi.org/10.1016/j.atmosenv.2007.10.058, 2007

Williams, J. E., Boersma, K. F., Sager, P. L., & Verstraeten, W. W. : The high-resolution version of TM5-MP for optimized satellite retrievals: description and validation. Geosci. Model Dev.t, 10(2), 721-750. doi:https://doi.org/10.5194/gmd-10-721-2017, 2017

Wittrock, F., Richter, A., Oetjen, H., Burrows, J. P., Kanakidou, M., Myriokefalitakis, S., Volkamer,R., Berlie,S., Platt,U., & Wagner, T. : Simultaneous global observations of glyoxal and formaldehyde from space. Geophys. Res. Lett., 33(16). doi:https://doi.org/10.1029/2006GL026310, 2006

Wofsy, S. C., Afshar, S., Allen, H. M., Apel, E., Asher, E. C., Barletta, B., Bent, J., Bian, H., Biggs, B. C., Blake, D. R., Blake, N., Bourgeous, I., Brock, C. A., Brune, W. H., Budney, J. W., Bui, T. P., Butler, A., Campuzano-Jost, P., Chang, C. S., Chin, M., Commane, R., Correa, G., Crounse, J. D., Cullis, P. D., Daube, B. C., Day, D. A., Dean-Day, J. M., Dibb, J. E., DiGangi, J. P., Diskin, G. S., Dollner, M., Elkins, J. W., Erdesz, F., Fiore, A. M., Flynn, C. M., Froyd, K., Gesler, D. W., Hall, S. R., Hanisco, T. F., Hannun, R. A., Hills, A. J., Hintsa, E. J., Hoffman, A., Hornbrook, R. S., Huey, L. G., Hughes, S., Jimenez, J. L., Johnson, B. J., Katich, J. M., Keeling, R., Kim, M. J., Kupc, A., Lait, L. R., Lamarque, J.-F., Liu, J., McKain, K., McLaughlin, R. J., Meinardi, S., Miller, D. O., Montzka, S. A., Moore, F. L., Morgan, E. J., Murphy, D. M., Murray, L. T., Nault, B. A., Neuman, J. A., Newman, P. A., Nicely, J. M., Pan, X., Paplawsky, W., Peischl, J., Prather, M. J., Price, D. J., Ray, E., Reeves, J. M., Richardson, M., Rollins, A. W., Rosenlof, K. H., Ryerson, T. B., Scheuer, E., Schill, G. P., Schroder, J. C., Schwarz, J. P., St. Clair, J. M., Steenrod, S. D., Stephens, B. B., Strode, S. A., Sweeney, C., Tanner, D., Teng, A. P., Thames, A. B., Thompson, C. R., Ullmann, K., Veres, P. R., Vieznor, N., Wagner, N. L., Watt, A., Weber, R., Weinzierl, B., Wennberg, P. O., Williamson, C. J., Wilson, J. C., Wolfe, G. M., Woods, C. T., and Zeng, L. H. : ATom: Merged Atmospheric Chemistry, Trace Gases, and Aerosols, Version 1.5, 2840.233496 MB. https://doi.org/10.3334/ORNLDAAC/1581, 2018

Yáñez-Serrano, A. M., E. Bourtsoukidis, E. G. Alves, M. Bauwens, T. Stavrakou, J. Llusià, I. Filella, A. Guenther, J. E. Williams and P. Artaxo : Amazonian biogenic volatile organic compounds under global change, Glob. Chang. Biol. , 26(9): 4722-4751, https://doi.org/10.1111/gcb.15185, 2020

Zara, M., Boersma, K. F., De Smedt, I., Richter, A., Peters, E., Van Geffen, J. H. G. M., Beirle, S., Wagber, T., Van Roozendael, M., & Marchenko, S. : Improved slant column density retrieval of nitrogen dioxide and formaldehyde for OMI and GOME-2A from QA4ECV: intercomparison, uncertainty characterization, and trends. Atmos. Meas. Tech., 11(7), 4033-4058. doi:https://doi.org/10.5194/amt-11-4033-2018,2018

Zhao, T., Mao, J., Simpson, W. R., De Smedt, I., Zhu, L., Hanisco, T. F., Wolfe, G. M. ,St. Clair, J. M., González Abad, G., Nowlan, C. R., Barletta, B., Meinardi, S., Blake, D. R., Apel, E. C., & Hornbrook, R. S. : Source and variability of formaldehyde (HCHO) at northern high latitudes: an integrated satellite, aircraft, and model study. Atmos. Chem. Phys., 22(11), 7163-7178. doi:10.5194/acp-22-7163-2022, 2022

Supplementary Information

Evaluating CHASER V4.0 global formaldehyde (HCHO) simulations using satellite, aircraft, and ground-based remote sensing observations

Hossain Mohammed Syedul Hoque[1], Kengo Sudo[1,2], Hitoshi Irie[3], Yanfeng He[1], and Md Firoz Khan[4]

[1]Graduate School of Environmental Studies, Nagoya University, Nagoya, 4640064, Japan

[2]Japan Agency for Marine-Earth Science and Technology (JAMSTEC), Kanagawa, 2370061, Japan

[3]Center for Environmental Remote Sensing (CEReS), Chiba University, Chiba,2638522, Japan

[4]Department of Environmental Science and Management, North South University, Bangladesh

Correspondence to: Hossain Mohammed Syedul Hoque (hoquesyedul@gmail.com; hoque.hossain.mohammed.syedul.u6@f.mail.nagoya-u.ac.jp)

1. Impact of model resolution and other model error sources.

The coarse horizontal and vertical resolution can lead to additional errors related to atmospheric transport and chemical processes. Seasonal variations in the HCHO levels in different regions, simulated at 1.4° × 1.4° resolution, are compared with the standard simulations in Fig S1. The statistics are listed in Table S1.

Except for the Indian regions, both simulations' absolute values are similar. The MBE between the two simulations over the Indian regions (IGP, S-India, and N-India) is ~ 2×10^{15} molecules cm^{-2}. Over E-India and S-India, the MBE between the standard simulation TROPOMI observations is ~1.5×10^{15}molecules cm^{-2}. This signifies that high-resolution simulations will reduce the model-observation MBE in these regions by at least ~25%.

Chemical kinetics described in the model can also induce uncertainties. The simulations do not consider direct emissions of HCHO from anthropogenic and pyrogenic sources. Photolysis of glyoxal, the most abundant di-carbonyl in the atmosphere, is a crucial HCHO production pathway (Vrekoussis et al., 2010). The current CHASER VOC scheme doesn't include glyoxal reactions and byproducts. Simulations with updated VOC chemistry schemes and emission inventories will be addressed in detail in a separate article.

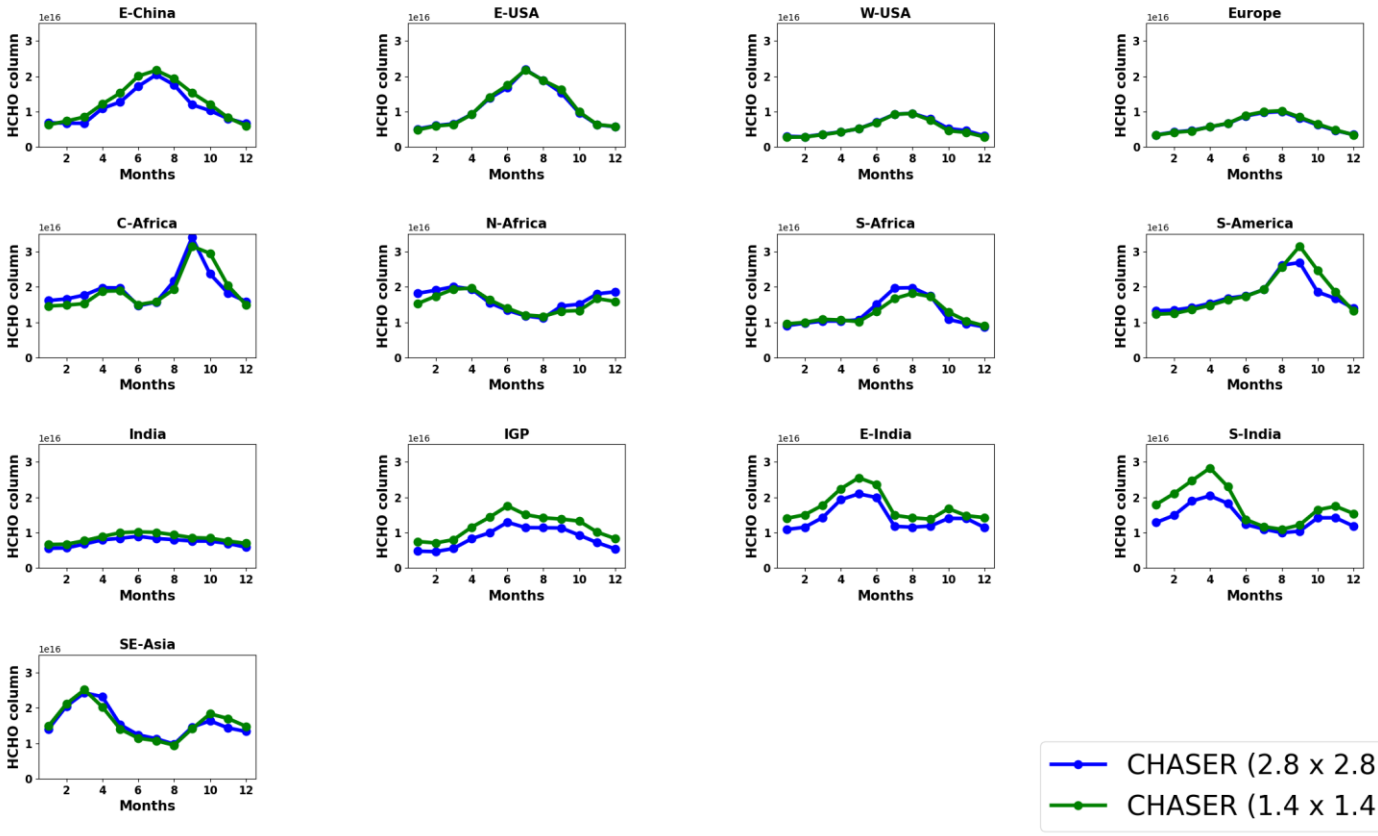

Figure S1. Monthly variations in HCHO columns in the selected regions, simulated at 2.8˚× 2.8˚ (blue, standard simulation) and 1.4˚ × 1.4˚ resolutions (green, high resolution). The coordinate bounds are similar to Fig.2.

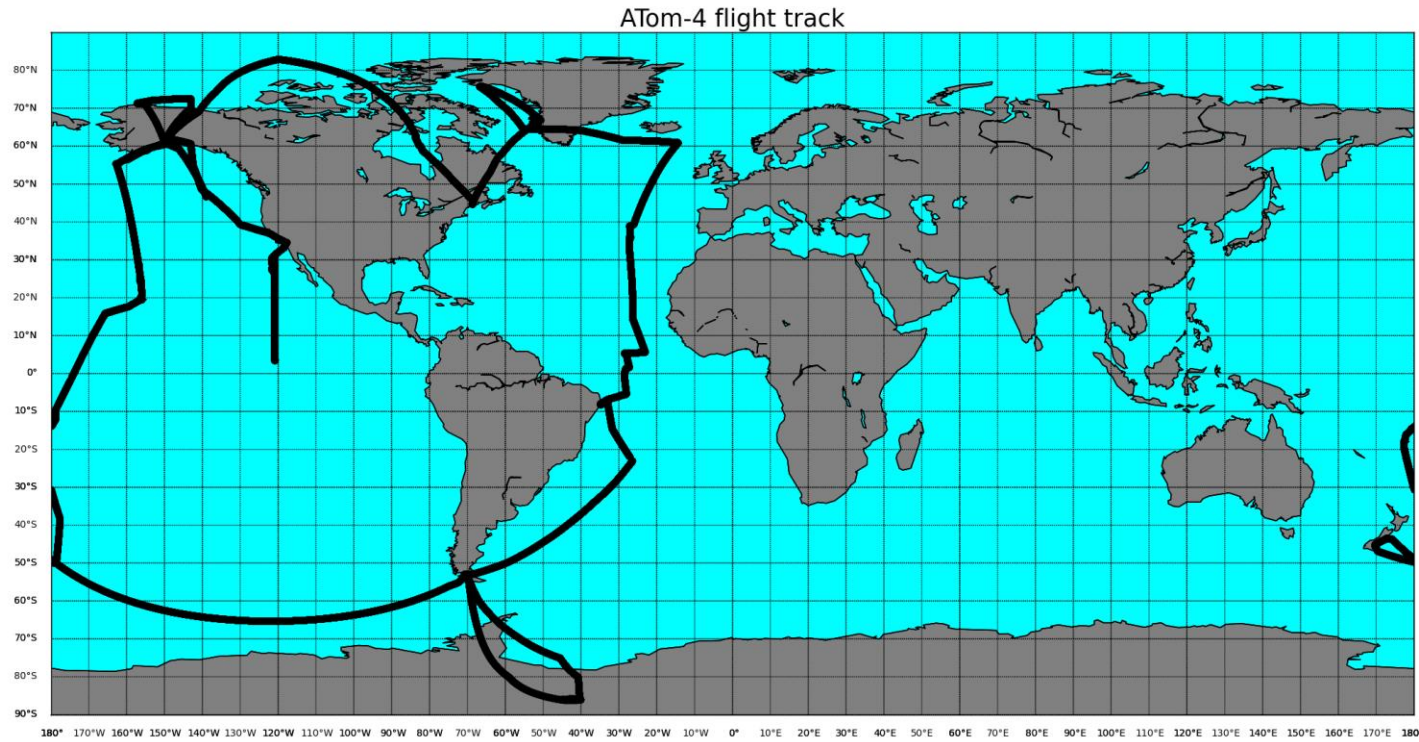

Figure S2. Atom-4 flight track.

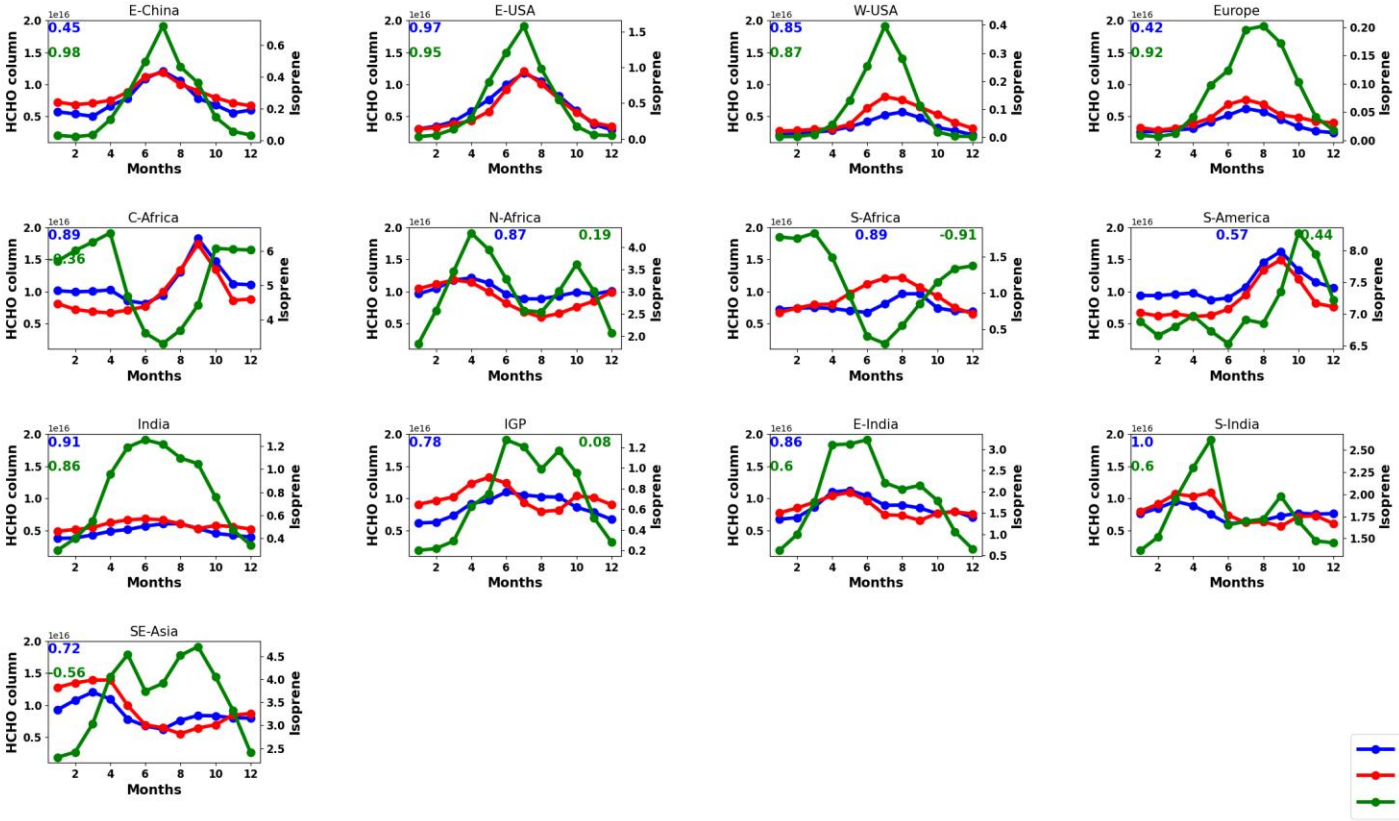

Figure S3. Seasonal variation in HCHO columns (× 10^{16} molecules cm^{-2}) in eastern China (E-China; 30–40°N, 110–123°E), eastern United States (E-USA; 32–43°N,95–71°W), western United States (W-USA; 32–43°N, 125–100°W), Europe (35–60°N, 0–30°E), central Africa (C-Africa; 10–20°S, 60°W – 60°E), northern Africa (N-Africa; 5–15°N, 10°W–30°E), southern Africa (S-Africa; 5–15°S, 10–30°E), South America (S-America; 20°S – 0°N, 50–70° W), India (7.5–54°N, 68–97°E), the Indo Gangetic Plain (IGP; 21–33°N, 72–89°E), east India (E-India; 15–25°N, 80–90°E)), south India (S-India; 0–15°N, 63–80°E), and Southeast Asia (SE-Asia, 10–20°N, 96–105°E).The red, blue, and red lines are TROPOMI retrievals and CHASER simulations, respectively. The green curves signify the simulated isoprene seasonality in the respective regions. The blue number indicates the correlation between TROPOMI and CHASER HCHO columns, whereas the green number is the correlation between TROPOMI retrievals and isoprene concentrations. The unit of isoprene concentrations is ppbv.

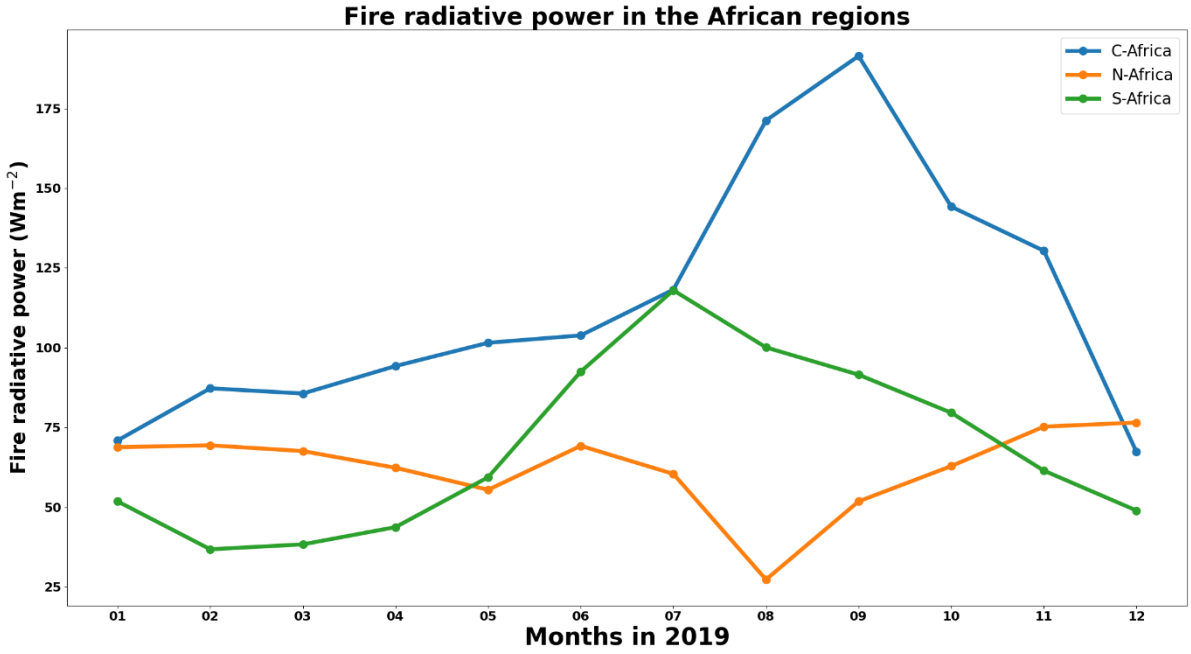

Figure S4. Monthly variations of fire radiative power (blue) and fire numbers (black curve) in the North African region. The fire data are extracted from the MODIS Active Fire Detections database (https://firms.modaps.eosdis.nasa.gov, last accessed on 2022/4/15). FRP retrieval confidence higher than 80% is plotted only.

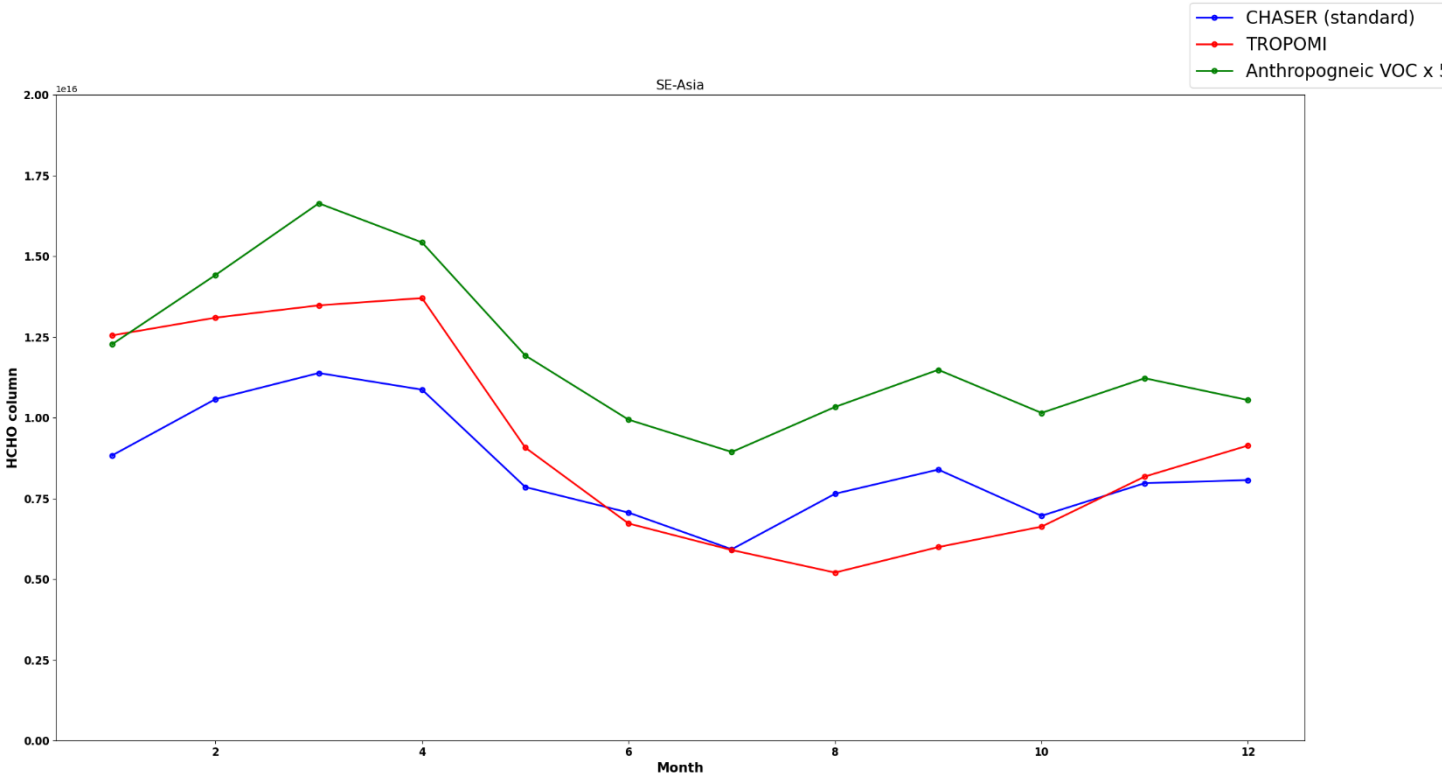

Figure S5. Seasonal variation of HCHO (x 10^{16} molecules cm^{-2}) in Southeast Asia, inferred from standard simulations (blue), TROPOMI observations (red), and ANI estimate (green). Anthropogenic VOC emissions are increased by fivefold in the ANI simulations. The coordinate bounds of Southeast Asia are similar to Fig. 2. The simulation setting is given in Table 1.

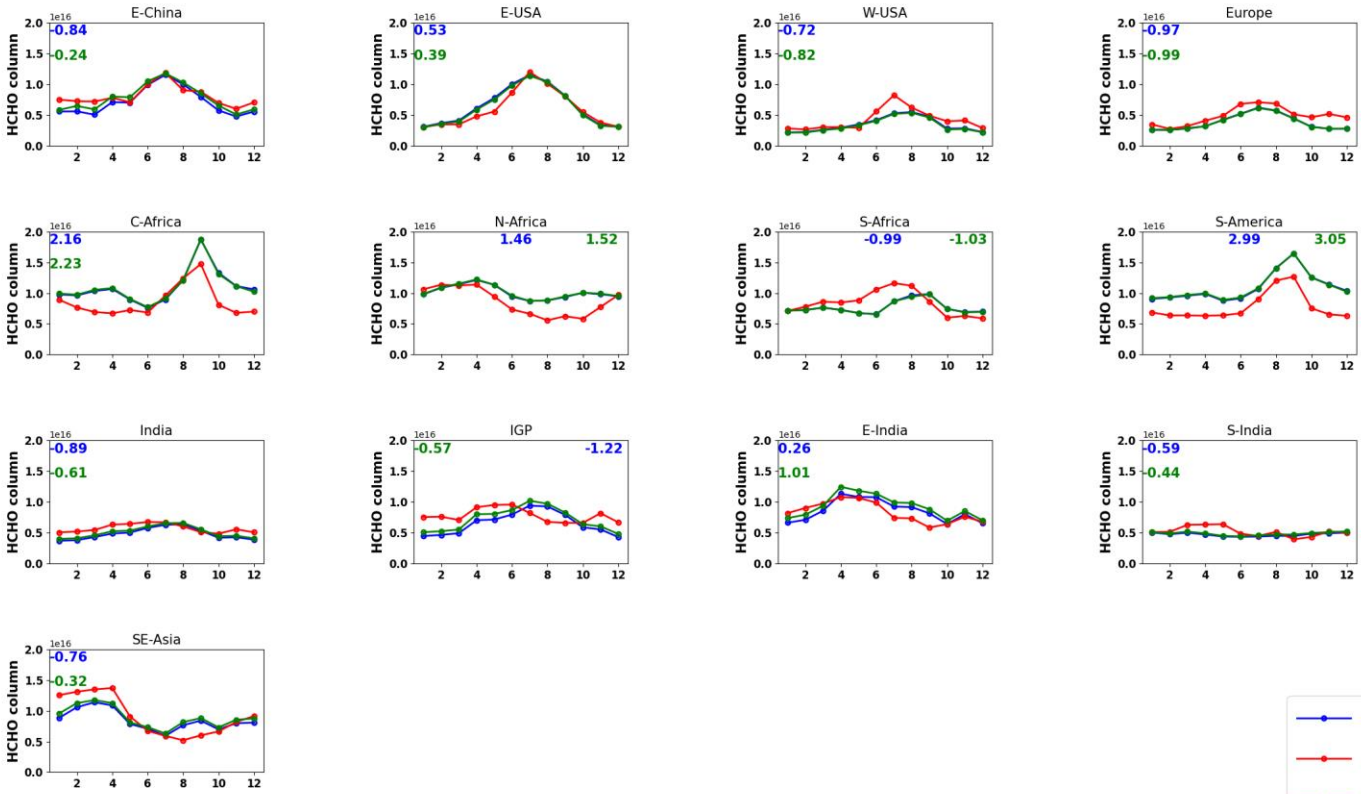

Figure S6. . Seasonal variation of HCHO (x 10^{16} molecules cm^{-2}) in the selected regions, inferred from standard simulations (blue), TROPOMI observations (red), and OLNE estimate (green). The HTAP-2008 NOx emission inventory is used in the OLNE simulations. The blue numbers indicate MBE between the TROPOMI and CHASER HCHO columns. The MBE between OLNE and TROPOMI columns are given in green colors. The coordinate bounds of the regions are similar to Fig. 2.

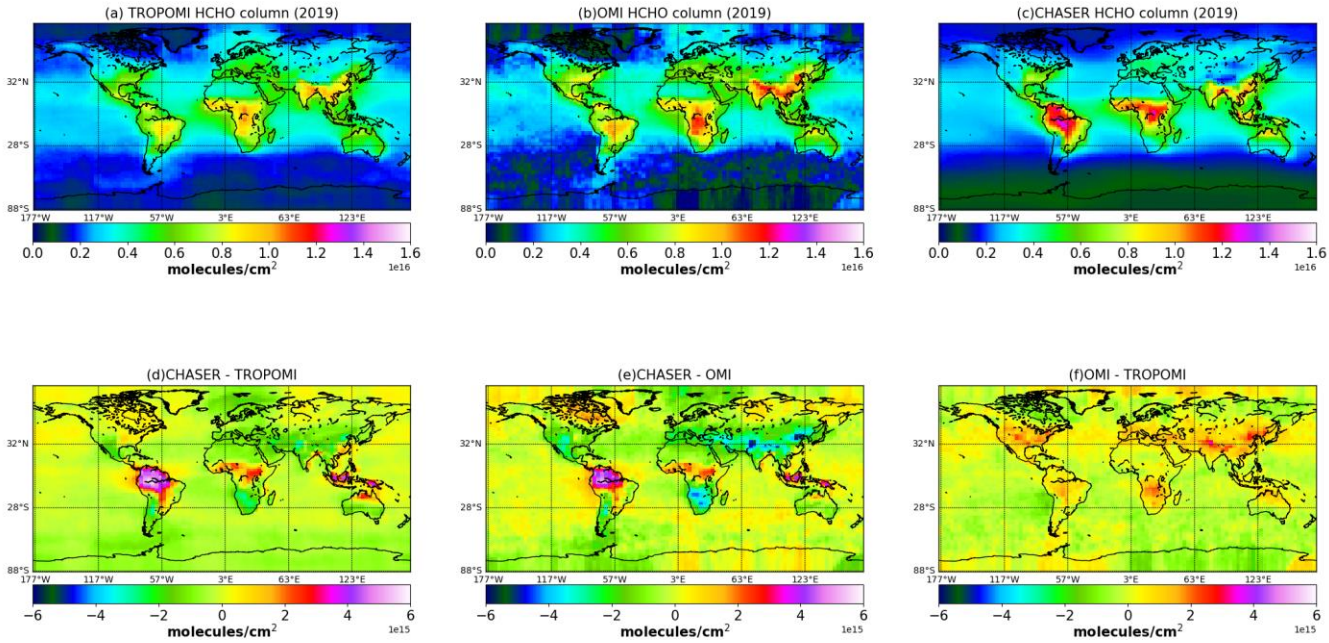

Figure S7. Annual (2019) mean HCHO columns (× 10^{16} molecules cm^{-2}) inferred from (a) TROPOMI and (b) OMI retrievals and (c) standard CHASER simulations. The differences between the two observational datasets are also plotted. The unit of difference is x 10^{15} molecules cm^{-2}.

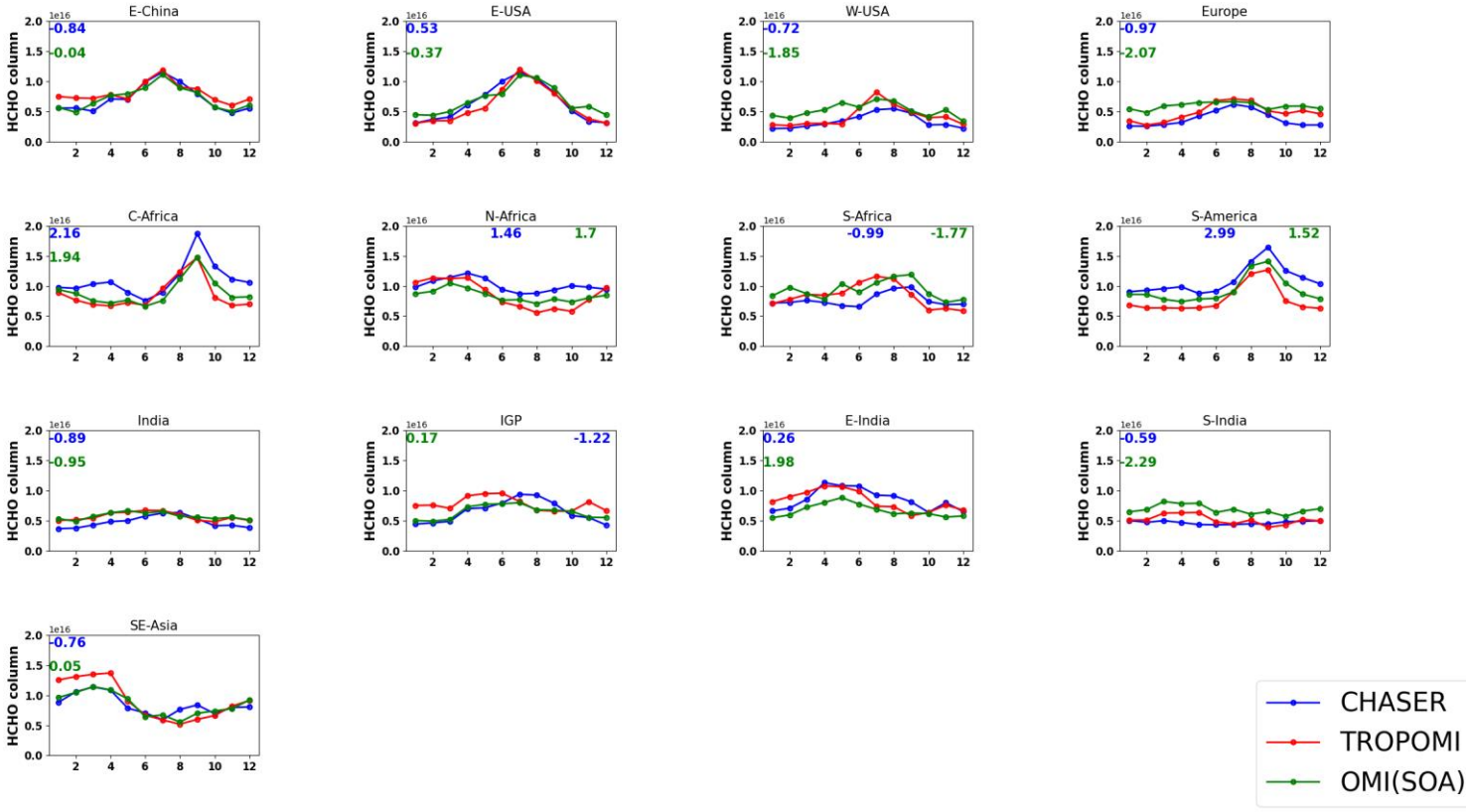

Figure S8: Seasonal variation of HCHO ($\times 10^{16}$ molecules cm^{-2}) inferred from TROPOMI (red curve) and OMI SOA (green curve) retrievals and standard CHASER (blue curves) simulations. The definition of the regions is the same as Fig.2. The blue numbers signify the MBE between TROPOMI and CHASER, whereas the green numbers are the MBE between CHASER and OMI SOA. Coincident dates among the datasets are used to calculate the monthly mean data.

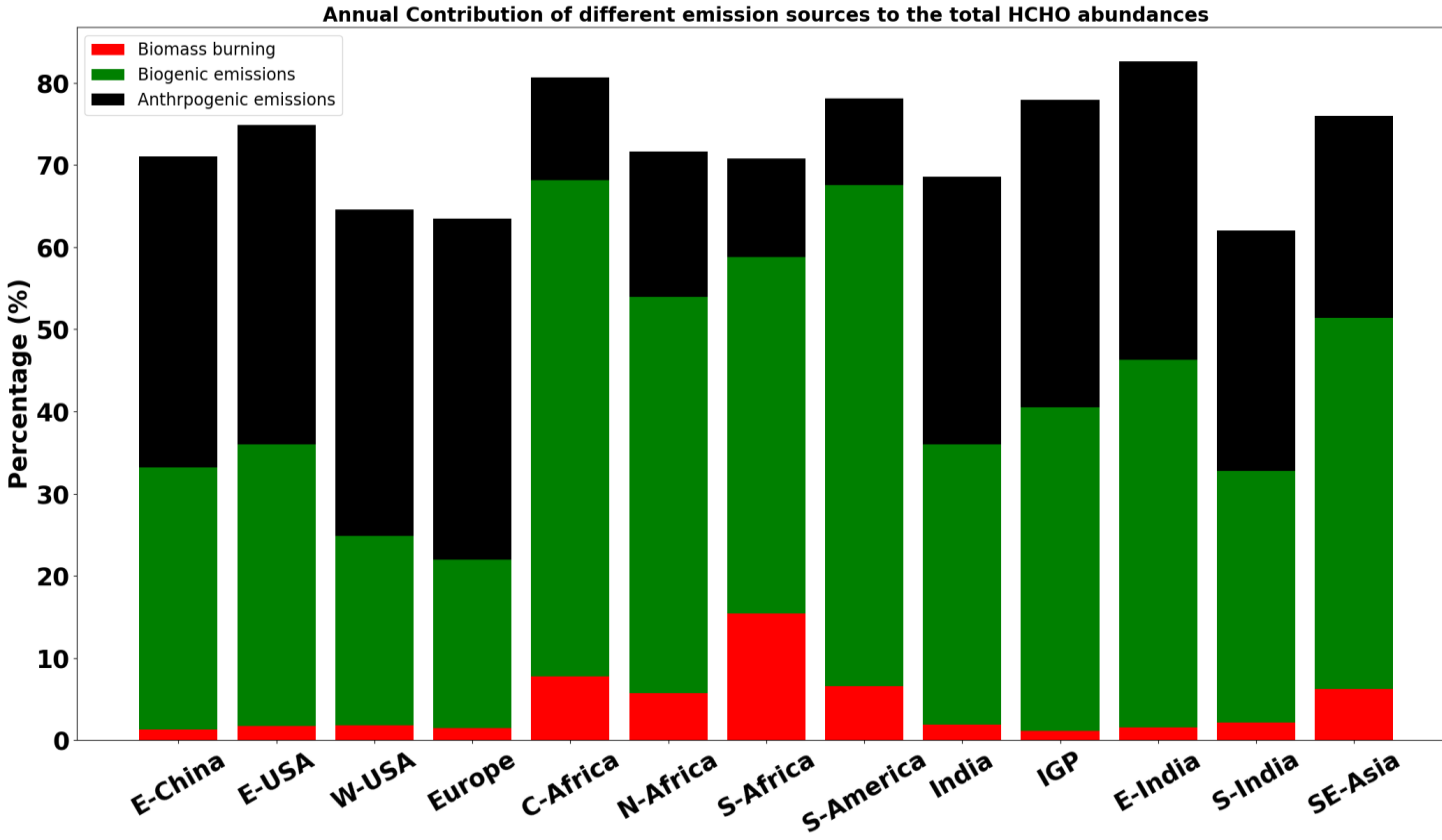

Figure S9: Annual relative contribution (%) of anthropogenic, pyrogenic, and biogenic emissions to the total HCHO column in the selected regions.

Table S1. Statistics of comparison between regional mean tropospheric HCHO simulations obtained from the standard and high-resolution simulations. Units of MBE (high resolution – standard simulation) and RMSE (high resolution – standard simulations) are $\times 10^{16}$ molecules cm^{-2}.

Region	MBE	RMSE
E-China	-0.09	0.12
E – USA	0.03	0.04
W-USA	0.03	0.03
Europe	0.00	0.01
C-Africa	0.10	0.11
N-Africa	0.14	0.18
S-Africa	0.05	0.08
S-America	0.07	0.07
India	-0.08	0.08
IGP	-0.21	0.22
S-India	-0.25	0.26

E-India	-0.27	0.30
SE-Asia	-0.03	0.11

Table S2. Monthly MBE and RMSE between satellite observations (TROPOMI and OMI) and CHASER simulations in 2019. Units of MBE and RMSE are $\times 10^{15}$ molecules cm^{-2}. Coincident date and time were used to calculate the statistics.

Month	**MBE1 (CHASER – TROPOMI)**	**MBE2 (CHASER – OMI)**	**RMSE1 (CHASER – TROPOMI)**	**RMSE2(CHASER – OMI)**
January	-0.17	-0.21	0.99	1.56
February	-0.12	-0.13	0.90	1.60
March	-0.23	-0.42	0.87	1.55
April	-0.25	-0.46	1.08	1.50
May	-0.25	-0.46	1.13	1.63
June	-0.30	-0.54	1.22	1.89
July	-0.28	-0.49	1.30	1.71
August	-0.23	-0.11	1.15	1.48

September	-0.20	0.00	1.21	1.48
October	-0.26	-0.19	1.40	1.92
November	-0.33	-0.02	1.32	1.87
December	-0.20	-0.70	1.21	2.31

Table S3. Comparison of annual mean background HCHO (× 10^{15} molecules cm^{-2}) columns obtained from IMAGES and CHASER simulations in 2019. MBE and RMSE are the abbreviated forms of mean bias error and root mean square error, respectively. Units of MBE and RMSE are ×10^{15} molecules cm^{-2}. Correlation signifies the spatial correlation between the datasets.

Year	Correlation	MBE	RMSE
2019	0.92	0.06	0.48

Table S4. Comparison of global mean HCHO columns (×10^{16} molecules cm^{-2}) obtained from TROPOMI observations, OMI BIRA retrieval, OMI SAO product, and CHASER simulations. Units of MBE and RMSE are ×10^{15} molecules cm^{-2}.

Region	MBE1 (Model–TROPOMI)	MBE2 (Model - OMI (BIRA))	MBE3(Model – OMI (SAO))	RMSE1 (Model - TROPOMI)	RMSE2 (Model - OMI(BIRA))	RMSE3 (Model – OMI(SAO))
Global	-0.23	-0.24	-1.49	0.77	0.99	1.76
E-China	-0.84	2.54	-0.04	1.40	3.03	1.25

E – USA	0.53	-1.02	-0.37	0.58	1.12	0.64
W-USA	-0.72	-2.09	-1.84	0.80	2.17	1.94
Europe	-0.97	-1.6	- 2.06	1.17	1.95	2.15
C-Africa	2.16	1.34	1.93	2.32	1.50	2.00
N-Africa	1.45	1.42	1.69	1.61	1.59	1.95
S-Africa	-0.99	-2.59	-1.76	1.32	2.75	2.07
S-America	2.98	2..02	1.52	3.41	2.61	1.80
India	-0.88	1.67	-0.94	1.31	2.26	1.98
IGP	-1.50	-2.46	0.99	1.56	2.51	1.13
S-India	0.26	0.05	1.97	1.22	1.38	2.54
E-India	-0.69	-0.59	-0.65	0.79	0.71	0.67
SE-Asia	-0.75	-0.83	0.04	1.16	1.14	1.07